Supplementary Information

Solution-Processable $Ni_3(HITP)_2$/MXene Heterostructures for ppb-Level Gas Detection

Xuanhao Wu‡ [a], Mengmeng Niu‡ [b], Xin Tian[c], Xiaoyan Peng[a], Pio John S. Buenconsej[d], Xu Wu[b], Yeliang Wang[b], Wei Ji[e], Yi Li[f], Jingsi Qiao* [b], Jifang Tao[c], Mingming Zhang[a], Song Xiao* [f] and Hongye Yuan* [a]

[a] State Key Laboratory for Mechanical Behavior of Materials, Shaanxi International Research Center for Soft Matter, School of Materials Science and Engineering, Xi'an Jiaotong University, Xi'an, 710049, P. R. China

[b] Advanced Research Institute of Multidisciplinary Sciences&School of Integrated Circuits and Electronics, Beijing Institute of Technology, Beijing 100081, China

[c] School of Information Science and Engineering, Shandong University, Qingdao, 266237, P. R. China.

[d] Facility for Analysis Characterization Testing Simulation (FACTS), Nanyang Technological University, 50 Nanyang Avenue, 639798, Singapore

[e] Beijing Key Laboratory of Optoelectronic Functional Materials & Micro-Nano Devices, Department of Physics, Renmin University of China, Beijing 100872, China

[f] State Key Laboratory of Power Grid Environmental Protection (School of Electrical Engineering and Automation), Wuhan University, Wuhan 430072, Hubei Province, China

‡ Contributed equally to this work

* Corresponding authors:

Hongye Yuan, E-mail: hongye.yuan@xjtu.edu.cn;

Jingsi Qiao , E-mail: qiaojs@bit.edu.cn (J.Q.);

Song Xiao, E-mail: xiaosong@whu.edu.cn (S.X.)

Table of Contents

Materials

The chemicals for the synthesis of MOF suspensions were purchased from commercial suppliers, including nickel nitrate hexahydrate ($Ni(NO_3)_2 \cdot 6H_2O$, purity > 98%, Sigma-Aldrich), 2,3,6,7,10,11-hexahydroxytriphenylene (HITP, purity > 97%, Macklin), multilayered MXene nanosheet dispersion in ethanol (Nb_2C, purity > 99%, 5 $g \cdot L^{-1}$, Xinxi Technology Co., Ltd.), ammonia solution (purity ≈ 30%, Sigma-Aldrich), and anhydrous ethanol (EtOH, purity > 99.8%, Sigma-Aldrich). All the chemicals were used without further purification.

Methods

Synthesis of $Ni_3(HITP)_2$/MXene Heterostructures and Powder

The synthesis process of $Ni_3(HITP)_2$/MXene suspensions involved several steps. Firstly, Nickel nitrate hexahydrate ($Ni(NO_3)_2 \cdot 6H_2O$, 50 mg) was dissolved in a mixed solution of anhydrous ethanol (25mL) and concentrated ammonia solution (2mL, 30%), and dissolving 2,3,6,7,10,11-hexaaminotriphenyl (HITP, 33 mg) in anhydrous ethanol (25mL), then mixing it and adding the multi-layer MXene (Nb_2C) nanosheet dispersion (5mL) to it. The synthesis took place at a temperature of 65 °C for a duration of 5 hours. The solution was composed of anhydrous ethanol (50 mL) and concentrated ammonia solution (2 mL, 30%). After synthesis, the resulting suspensions had a viscous consistency to remove impurities and unwanted by-products, the suspensions were rinsed five times with fresh anhydrous ethanol using a centrifuge operating at a speed of 8000 rpm. Subsequently, the rinsed suspensions were soaked in fresh anhydrous ethanol overnight. To further purify the suspensions, they were soaked in absolute ethanol for an additional two days, with the solvent being renewed periodically. Finally, the washed $Ni_3(HITP)_2$/MXene suspension was subjected to vacuum drying at a temperature of 150 °C. This drying process resulted in the formation of $Ni_3(HITP)_2$/MXene powder. Additionally, the reaction container we used was a 100 ml hydrothermal reaction

vessel with an inner lining made of polytetrafluoroethylene (PTFE). This container is characterized by its resistance to strong acids and bases, high temperature, and airtightness.

Synthesis of $Ni_3(HITP)_2$ Suspensions and Powder

$Ni_3(HITP)_2$ suspensions were synthesized by reacting a mixture solution containing HITP (33 mg) and $Ni(NO_3)_2 \cdot 6H_2O$ (50 mg) at 65 °C for 5 hours. The solution was composed of anhydrous ethanol (50 mL) and concentrated ammonia solution (2 mL, 30%). The resulting suspension was washed five times with fresh anhydrous ethanol using a centrifuge at a speed of 8000 rpm, then soaked in fresh anhydrous ethanol overnight. The washed $Ni_3(HITP)_2$ suspension was dried under vacuum at 150 °C to obtain $Ni_3(HITP)_2$ powder.

Fabrication of $Ni_3(HITP)_2$/MXene and MXene Monodispersed nanosheets

A suspension of alcoholic $Ni_3(HITP)_2$/MXene or MXene, with a concentration of 0.5 g L^{-1} and a volume of 20 μL, was meticulously applied onto a pristine silicon wafer or a copper mesh using the drop-casting. Subsequently, the sample was subjected to a drying process at a temperature of 80 °C for a duration of 20 minutes. This drying step effectively removed a significant portion of the solvent present in the sample. Following the initial drying process, the sample underwent a slow drying process under vacuum conditions for a period of one day. This extended drying period allowed for the gradual removal of any remaining solvent, resulting in the formation of uniformly monodispersed nanosheets of $Ni_3(HITP)_2$/MXene and MXene. These can be used for SEM and TEM characterizations. The slow drying process under vacuum conditions is essential for promoting the uniform distribution and arrangement of the nanosheets, which contributes to their overall quality and monodispersity.

Fabrication of $Ni_3(HITP)_2$/MXene Films

$Ni_3(HITP)_2$/MXene films on Si substrates were fabricated just via drop-casting. Typically, Si substrates were thoroughly rinsed by absolute ethanol twice under fierce stirring with each

circle for 10 min, afterward dried at 80 °C under ambient pressure. A certain volume of $Ni_3(HITP)_2$/MXene ethanol suspension was then captured by pipette and vertically dropped onto Si surfaces. $Ni_3(HITP)_2$/MXene films can thus be formed along with the vaporization of ethanol. For the film fabricated on polyvinylidene fluoride (PVDF) substrate: the PVDF substrate was blew with N_2 gas gun to remove surface dust. The pre-treated PVDF substrate was placed on an automatic film coater. Viscous $Ni_3(HITP)_2$/MXene alcoholic suspension with a concentration of 5 $g \cdot L^{-1}$ and a volume of 8 mL was dropped by pipette onto the PVDF substrate. Afterward, doctor-blading with a set height of 10 μm was performed at a speed of 1.0 $cm \cdot s^{-1}$ on the PVDF substrate. For the chip-level integration of $Ni_3(HITP)_2$/MXene films, chips were thoroughly cleaned twice by anhydrous ethanol without stirring. Each rinsing circle was kept for 10 min, and the chips were dried at 80 °C under ambient pressure. Relevant $Ni_3(HITP)_2$/MXene suspensions in ethanol with the same solid concentration (0.8 $g \cdot L^{-1}$) and volume (20 μL) were drop-casted onto the chips. Drying for all kinds of films was conducted at the ambient condition to fully vaporize the solvent, affording flat films.

Design and Fabrication of sensors

Platinum (Pt) interdigitated electrodes (IDEs) were produced and structured on silicon (Si) (100) wafers utilizing established cleanroom techniques, as documented in a previous publication[1]. The fabrication process involved precise patterning of Pt material on the Si wafers to create the interdigitated electrode configuration. Furthermore, a Pt micro-hotplate was integrated beneath the top IDEs, serving as a micro-heater. This micro-heater had the potential to activate the metal-organic framework (MOF) films in-situ. After the fabrication process, the wafers were diced into individual chips. These chips were then soldered onto printed circuit boards (PCB) to establish electrical connections. The wire coupling process, which involved connecting the IDEs to the relevant circuitry, was carried out subsequent to the soldering of the chips.

Theoretical Calculations

Density functional theory (DFT) calculations were performed using the generalized gradient approximation (GGA) for the exchange-correlation potential, the projector augmented wave (PAW) method[2-3], and a plane-wave basis set as implemented in the Viennaab initio simulation package(VASP)[4-5]. Van der Waals interaction were considered at the van der Waals density functional (vdW-DF) level with the optB86b functional (optB86b-vdW)[6]. The heterostructure consitsted of a monolayer $Ni_3(HITP)_2$ and a 7 × 7 bilayer Nb_2C superlattice with a vacuum layer of approximately 35 Å, and the lattice mismatch between $Ni_3(HITP)_2$ and the MXene is less than 0.7%. In structural relaxations, all atoms were fully relaxed until the residual force on every atom was less than 0.05 $eV \cdot Å^{-1}$. The kinetic energy cut off for the plane-wave basis was set to 500 eV. The adsorption energy was derived as follow: $E_{ads} = E_{molecule + substrate} - E_{substrate} - E_{molecule}$, where E_{ads} is the adsorption energy, $E_{molecule + substrate}$ is the total energy of adsorption geometry. $E_{substrate}$ and $E_{molecule}$ is the energy of an individual substrate and the isolated molecule, respectively.

Gas Sensing Tests

The gas sensing performance of the sensors based on $Ni_3(HITP)_2$/MXene films was evaluated by measuring the resistance change before and after gas adsorption. During the measurement process, the chip was placed in a custom chamber with stretchable metal contacts. Before data acquisition, the chamber was purged with nitrogen (N_2) for 15 minutes to stabilize the baseline resistance. N_2 was also used as a diluent to reach the target concentration and for sensor regeneration. The flow rate of all gases was kept constant at 100 sccm. A simplified scheme of the experimental set-up is available in the Figure S19.

The response was defined as the value obtained by sensor electrically-transduced signal changes in detected gas and purging gas (Δ (saturated signal change in gaseous

analytes)/(signal baseline in purging gas)). For example, the response of $Ni_3(HITP)_2$/MXene and $Ni_3(HITP)_2$ resistive sensor toward EtOH in air can be obtained by Eq. S1,

$$\text{Response}=\frac{|\Delta R|}{R_{air}}=\frac{|R_{gas}-R_{air}|}{R_{air}} \qquad \text{Eq. S1}$$

In order to determine the detection limit of the $Ni_3(HITP)_2$/MXene and $Ni_3(HITP)_2$ resistive sensor toward EtOH and NH_3, the standard deviation (SD) of the relevant response was calculated according to Eq. S2[7],

$$\text{SD}=\sqrt{\frac{\sum_{i=1}(y_a-y_{a*})^2}{n-2}} \qquad \text{Eq. S2}$$

in which y_a and y_{a*} denote the experimental and fitted responses, respectively, under the same EtOH or NH_3 concentration; n stands for the total points tested. The derived SD was then multiplied by a factor of 3, which was assigned to the relevant response upon exposure to the limit of detection of EtOH or NH_3. As such, the limit of detection can be derived by mapping the fitted curve as shown in Figure 2 (e) and 2 (f), i.e., EtOH (5 ppb) and NH_3 (250 ppb).

Characterizations

Fourier-transform infrared (FTIR) patterns were obtained by a Nicolet iS50 FTIR spectrometer. XPS spectrum obtained by ESCALAB Xi^+ X-ray photoelectron spectroscopy. Microstructural characterizations of $Ni_3(HITP)_2$/MXene nanosheets and relevant films, were characterized by scanning electron microscopy (SEM, SU8230) and X-ray diffractometer (XRD, Bruker) equipped with Cu Kα radiation (λ = 1.5406 Å) under a Bragg-Brentano geometry with a step size of 0.02° and a scan speed of $0.5°\cdot min^{-1}$. Two-dimensional (2D) grazing-incidence wide-angle X-ray scattering (GIWAXS) measurements were performed on Nanoinxider (Xenocs) with Cu Kα radiation as the source at an incidence angle of 0.2°. Transmission electron microscopy (TEM) imaging was conducted via a JEOL TEM (JEM-

2100). High angle annular dark field (HAADF)-STEM imaging was performed by a JEM-ARM200F (JEOL) microscope equipped with an ASCOR aberration corrector and a cold-field emission gun, operated at 200 kV. Focused ion beam coupled transmission electron microscopy (FIB-TEM) imaging was performed via a JEOL TEM coupled with a Ga ion beam. AFM tapping mode was used for the morphology and height analysis of $Ni_3(HITP)_2$/MXene and MXene nanosheets or films at room temperature. The measurements were performed on a Bruker Edge instrument with scanning rate at 0.7 Hz. N_2 sorption isotherms were collected under 77 K using a Micromeritics ASAP 2460 surface area and pore size analyzer. Measuring the conductivity of $Ni_3(HITP)_2$/MXene and MXene powder using the standard four electrode method, the set pressure ranges from 2.0 to 30.0 MPa.

Additional results

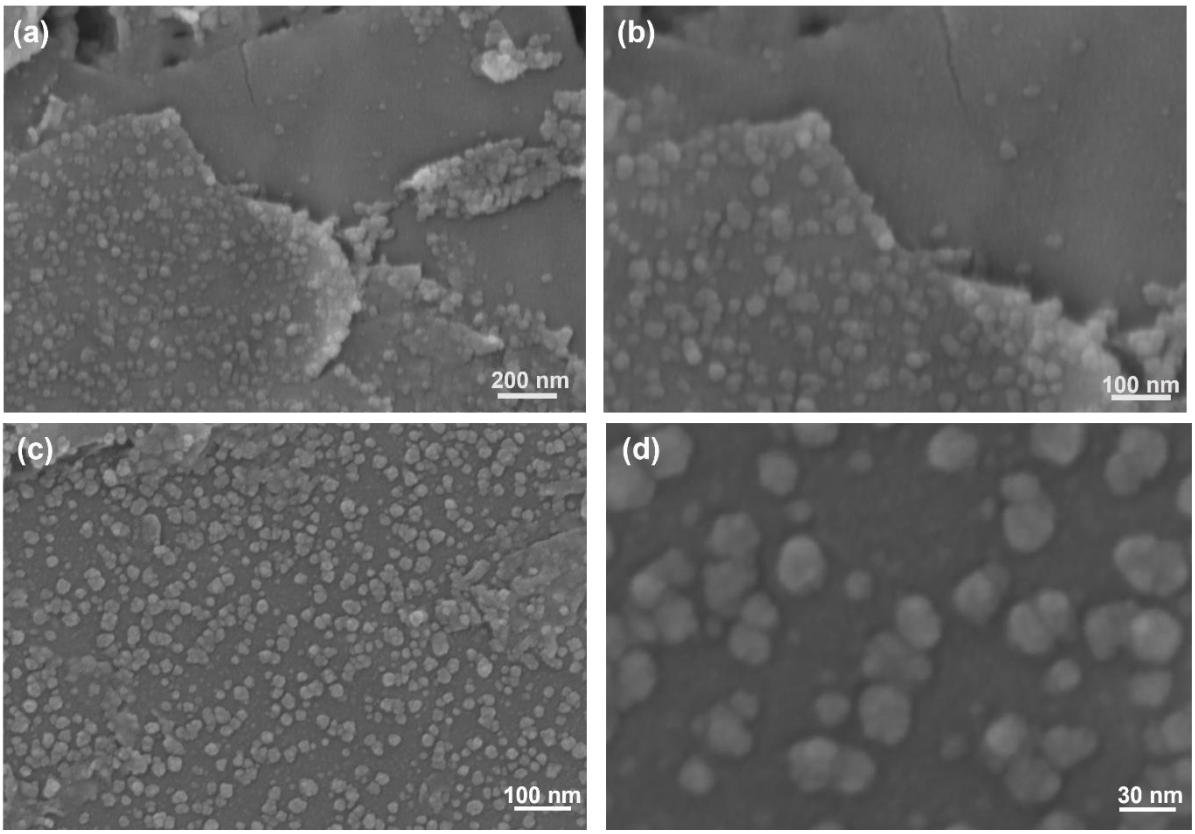

Figure S1. (a-b) SEM images of the $Ni_3(HITP)_2$/MXene heterostructure on a silicon substrate.

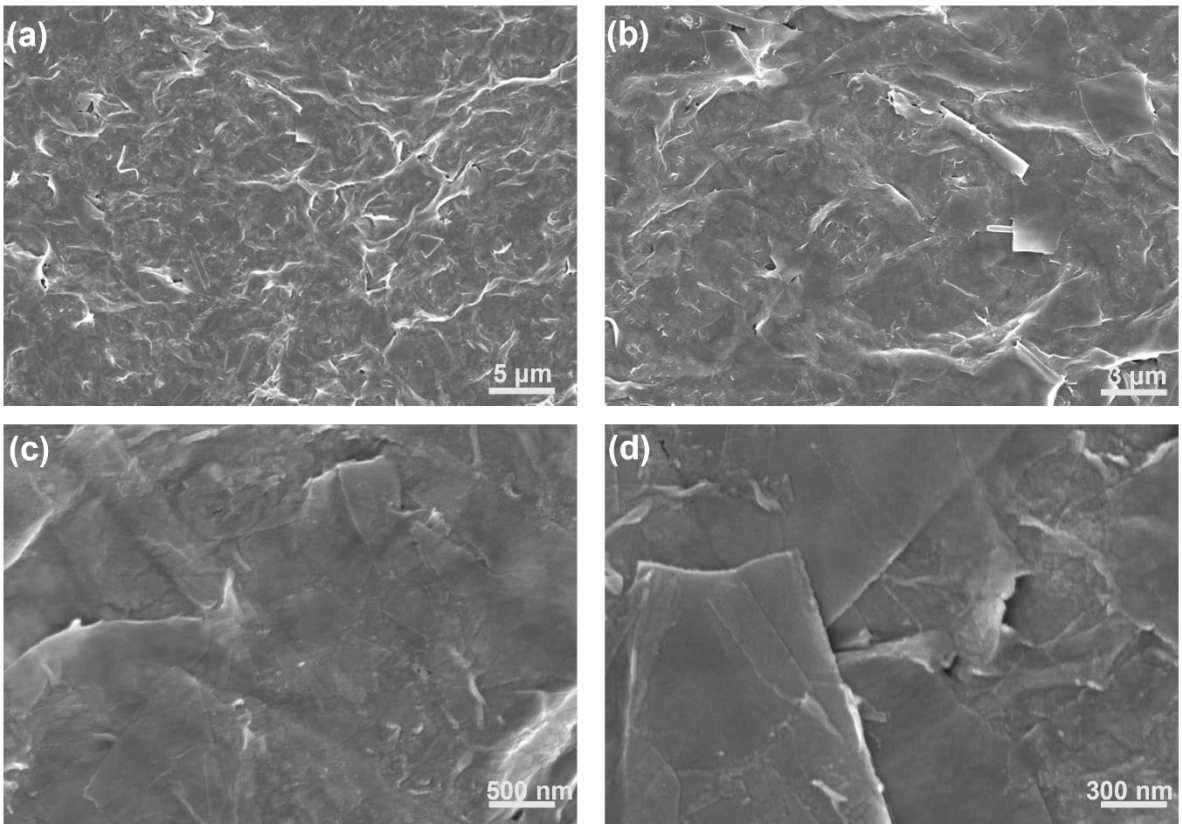

Figure S2. (a-d) SEM images of the MXene nanosheets on a silicon substrate.

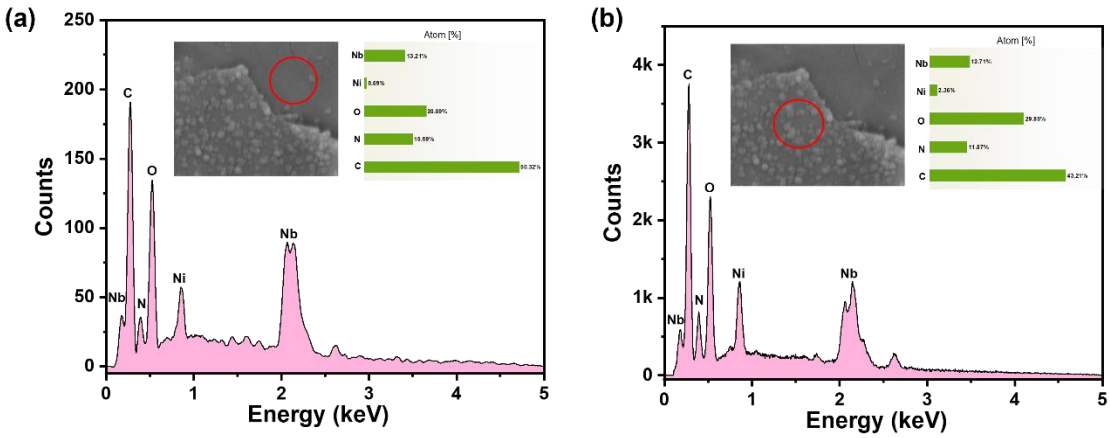

Figure S3. (a-b) Elemental composition and distribution on both sides of edge of the $Ni_3(HITP)_2$/MXene heterostructure: (a) MXene. (b) $Ni_3(HITP)_2$/MXene.

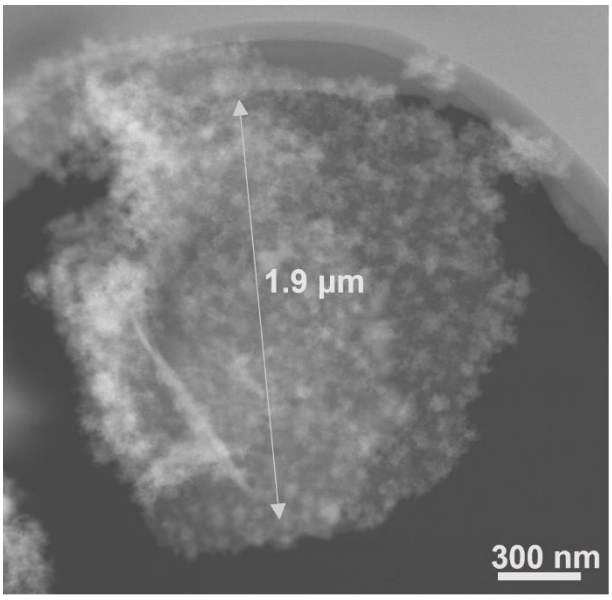

Figure S4. Low-magnification TEM image of the well-dispersed $Ni_3(HITP)_2$/MXene nanosheets.

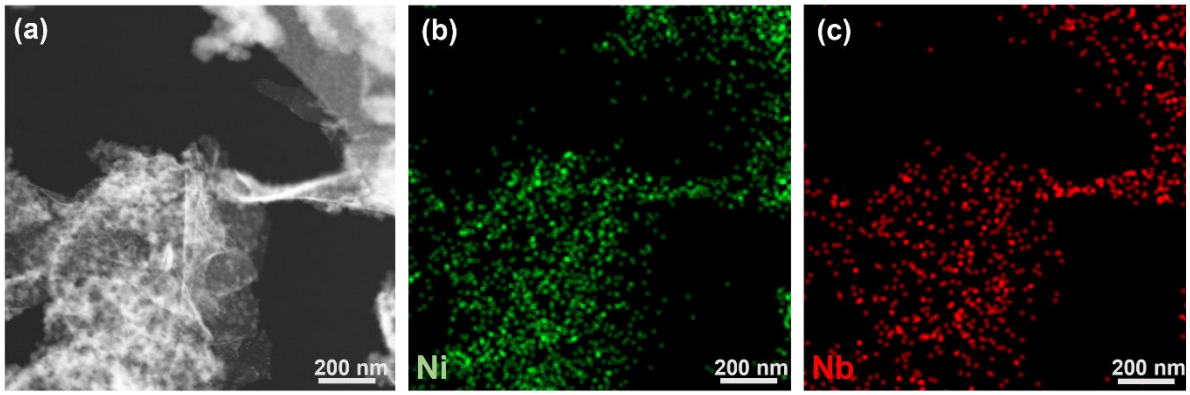

Figure S5. (a) Low-magnification TEM image of well-dispersed $Ni_3(HITP)_2$/MXene nanosheets. (b-c) The elemental Ni and Nb mapping images of the $Ni_3(HITP)_2$/MXene nanosheets.

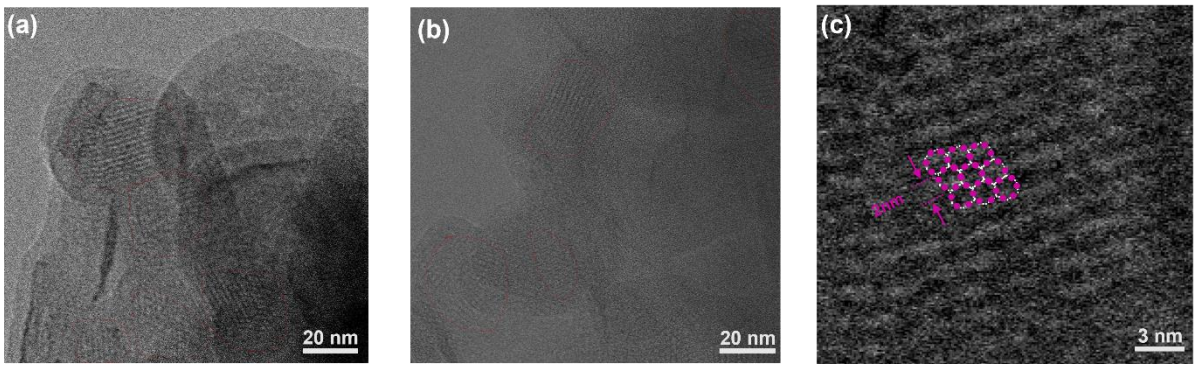

Figure S6. (a-c) STEM images of the $Ni_3(HITP)_2$/MXene nanosheet. Inset depicts the schematic illustration of the $Ni_3(HITP)_2$ framework viewed from *c*-direction.

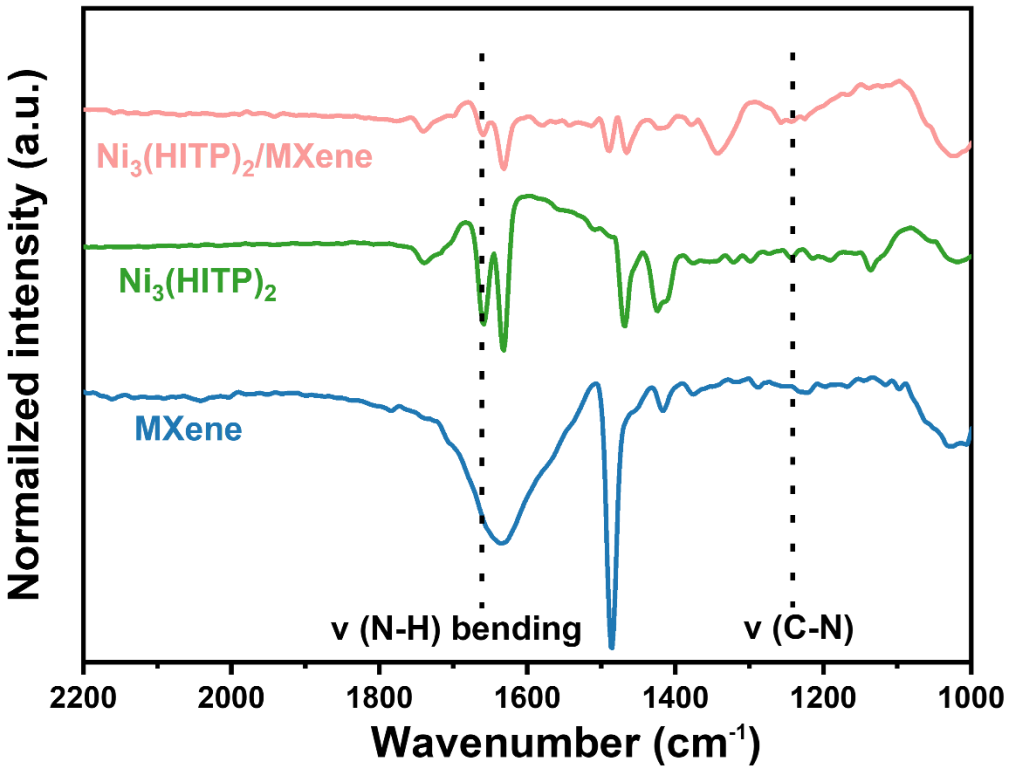

Figure S7. FTIR spectra comparison of the $Ni_3(HITP)_2$/MXene structure and MXene structure.

Note: Regarding the infrared spectra of the $Ni_3(HITP)_2$/MXene structure, in addition to the characteristic peaks attributed to MXene, we also observed peaks appearing in the infrared shift range of 1000-1600 cm^{-1}, which can be attributed to the vibration of C-C bonds in the HITP linker of $Ni_3(HITP)_2$, indicating the successful formation of the $Ni_3(HITP)_2$/MXene structure (Figure S1).

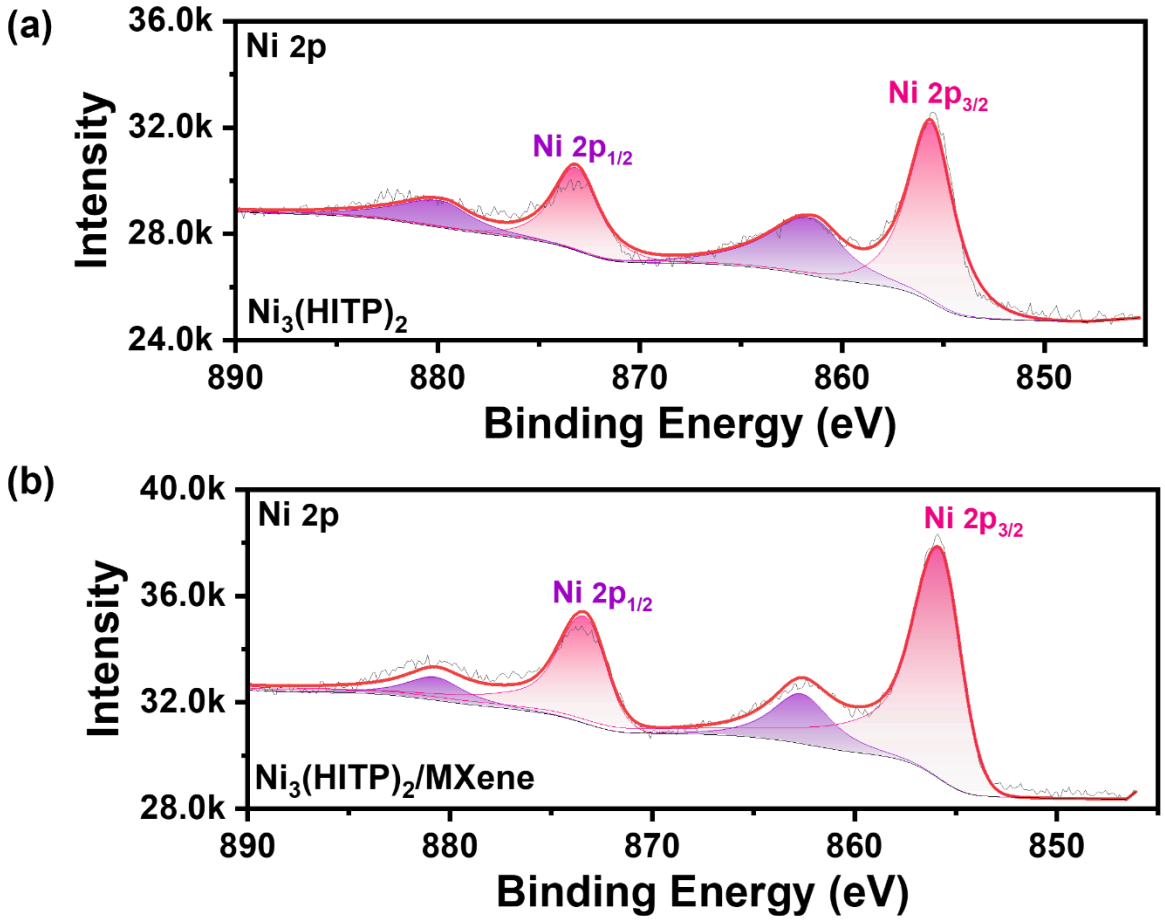

Figure S8. (a-b) Ni *2p* X-ray photoelectron spectroscopy (XPS) spectra of (a) $Ni_3(HITP)_2$ powder and (b) $Ni_3(HITP)_2$/MXene structure.

Note: The chemical environment of Ni in the $Ni_3(HITP)_2$/MXene structure and $Ni_3(HITP)_2$ powder was analyzed using XPS. From the XPS spectra, we observed no significant difference in the Ni *2p* spectra between $Ni_3(HITP)_2$/MXene and $Ni_3(HITP)_2$ powder, indicating that the chemical environment of Ni in these two samples is the same.

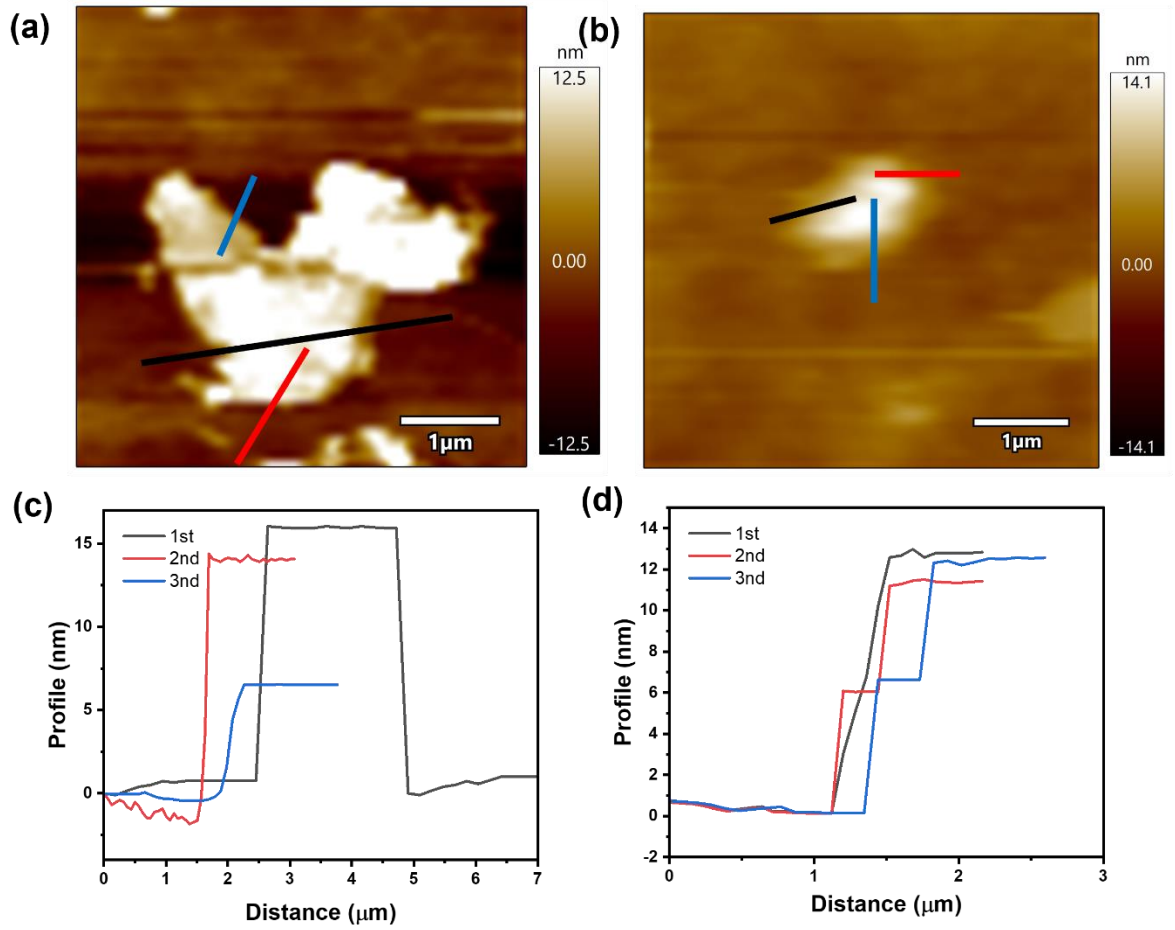

Figure S9. (a-b) Additional AFM images of monodispersed $Ni_3(HITP)_2$/MXene nanosheets on Si surfaces. (c-d) The second row presents the height profiles of (a-b), respectively.

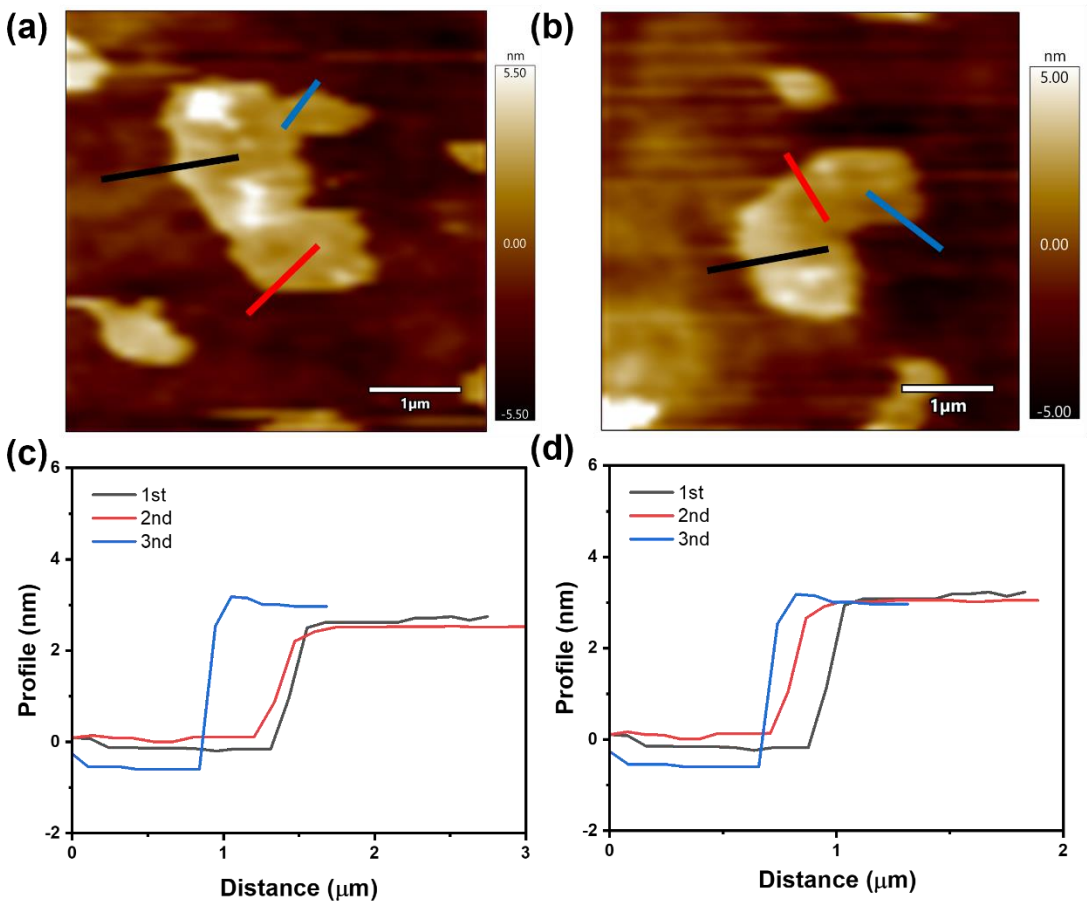

Figure S10. (a-b) Additional AFM images of monodispersed MXene nanosheets on Si surfaces. (c-d) The second row presents the height profiles of (a-b), respectively.

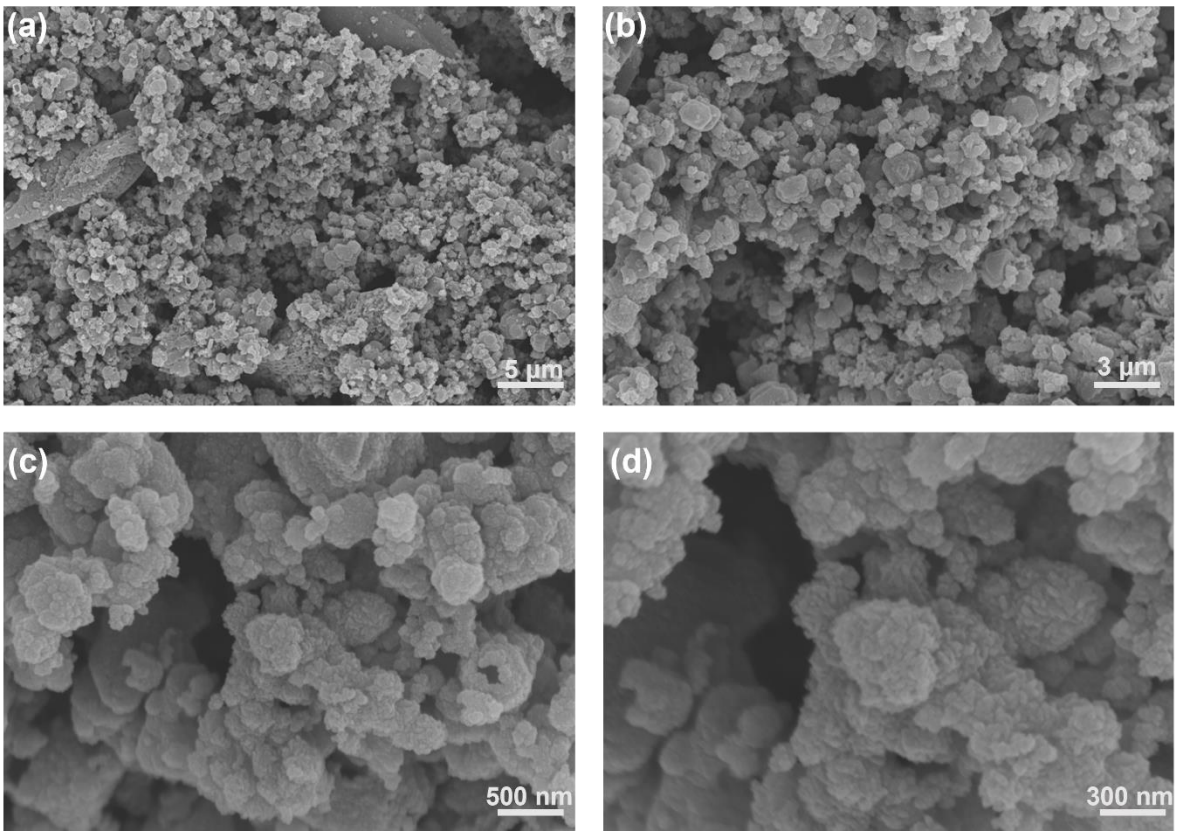

Figure S11. (a-d) SEM images of $Ni_3(HITP)_2$ powder obtained by the conventional hydrothermal method.

Note: The morphology of $Ni_3(HITP)_2$ powder was characterized using SEM. The $Ni_3(HITP)_2$ powder was placed on a clean silicon substrate and then mounted onto the sample holder of the SEM. SEM images of the $Ni_3(HITP)_2$ powder were collected at an accelerating voltage of 5 kV. The SEM images of the $Ni_3(HITP)_2$ powder sample exhibited irregularly arranged particulate crystals.

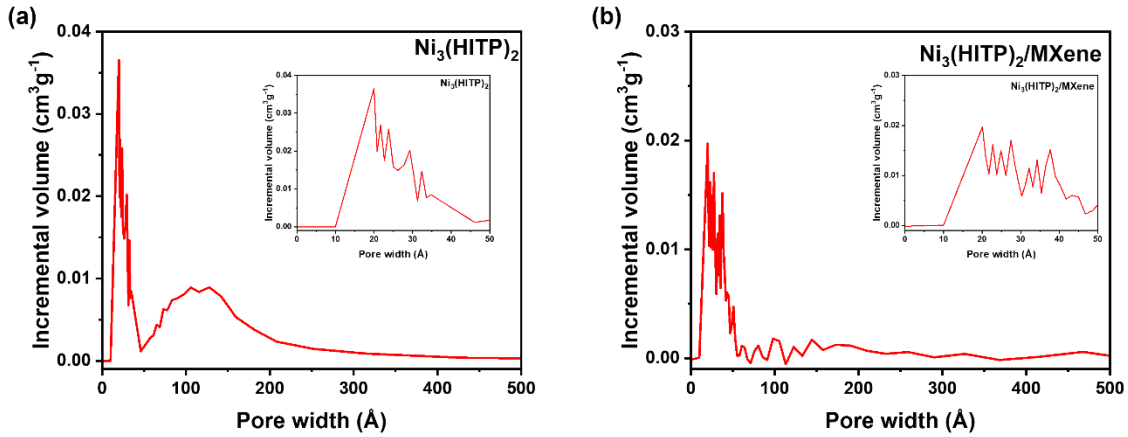

Figure S12. (a-b) Pore size distribution of the $Ni_3(HITP)_2$/MXene and $Ni_3(HITP)_2$ powder as shown in Figure 2i, respectively.

Note: The pore size distribution of both $Ni_3(HITP)_2$/MXene and $Ni_3(HITP)_2$ is mainly centered around 2 nm. However, there is a possible distribution of $Ni_3(HITP)_2$ pore size around 12 nm, which may be due to the gaps between the particles due to the stacking of $Ni_3(HITP)_2$.

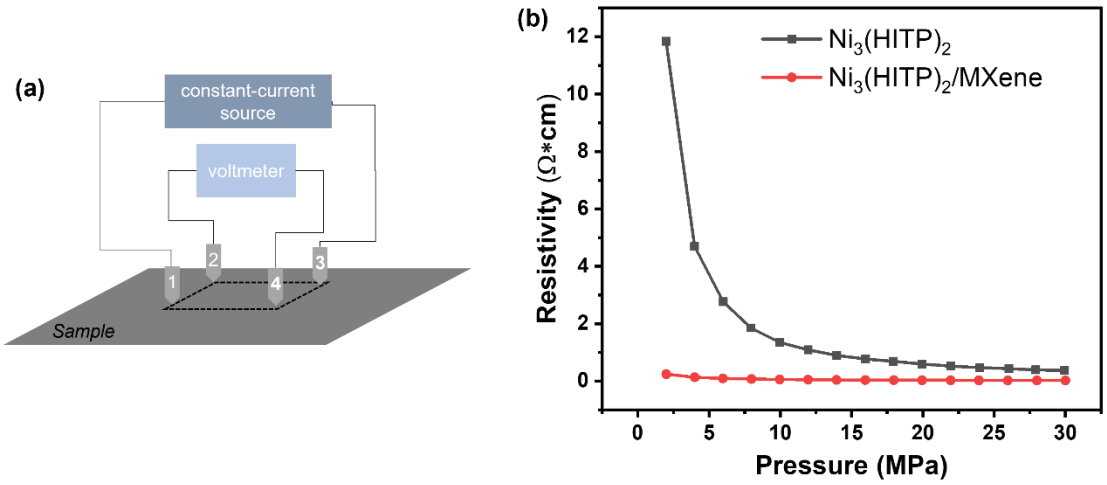

Figure S13. (a) Schematic diagram of the four-probe method for measuring resistance. (b) Resistivity curve of the $Ni_3(HITP)_2$/MXene hetorostructure and $Ni_3(HITP)_2$ powders measured by a standard four-point method as a function of pressure, respectively.

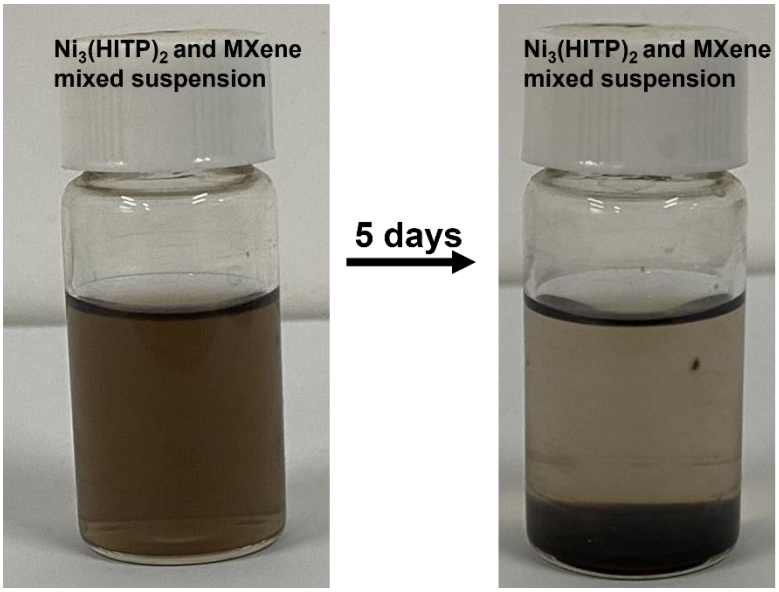

Figure S14. Optical photographs of $Ni_3(HITP)_2$/MXene and $Ni_3(HITP)_2$ mixed suspension both prior to and after being left at room temperature for a duration of five days.

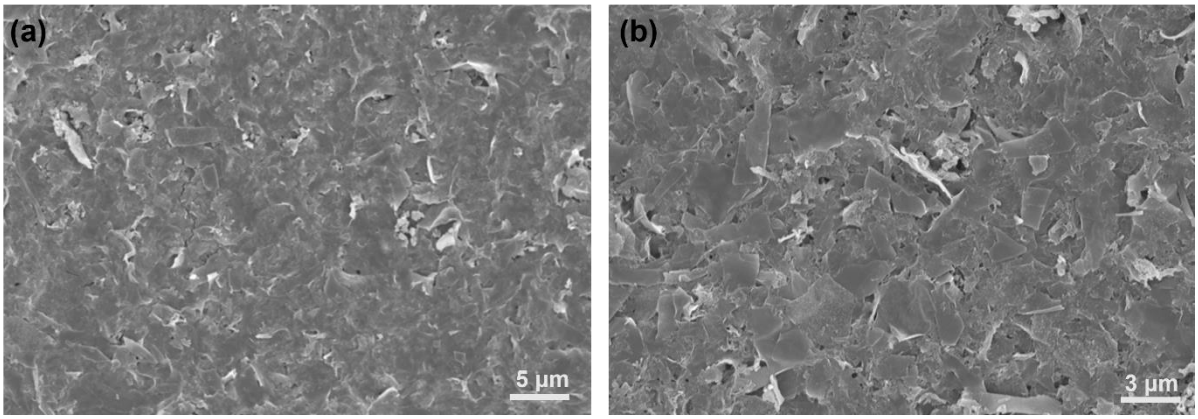

Figure S15. (a-b) Top-view SEM images of the $Ni_3(HITP)_2$/MXene films.

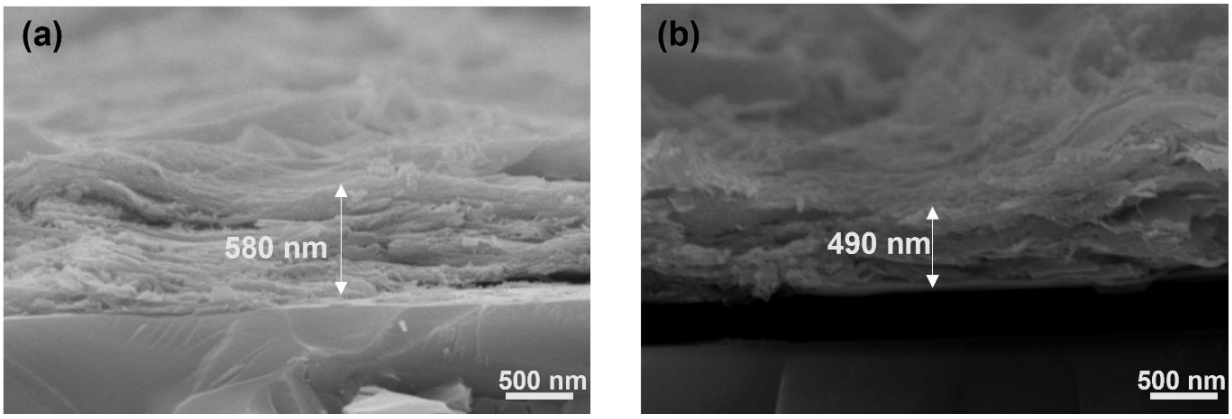

Figure S16. (a-b) Cross-sectional SEM images of a series of $Ni_3(HITP)_2$/MXene films on Si substrates with tunable thickness. Solid concentration and solution volume used for films: a) $C_{Ni_3(HITP)_2/MXene}$ = 1 g·L^{-1}, 20 µL; b) $C_{Ni_3(HITP)_2/MXene/MXene}$ = 0.8 g·L^{-1}, 20 µL.

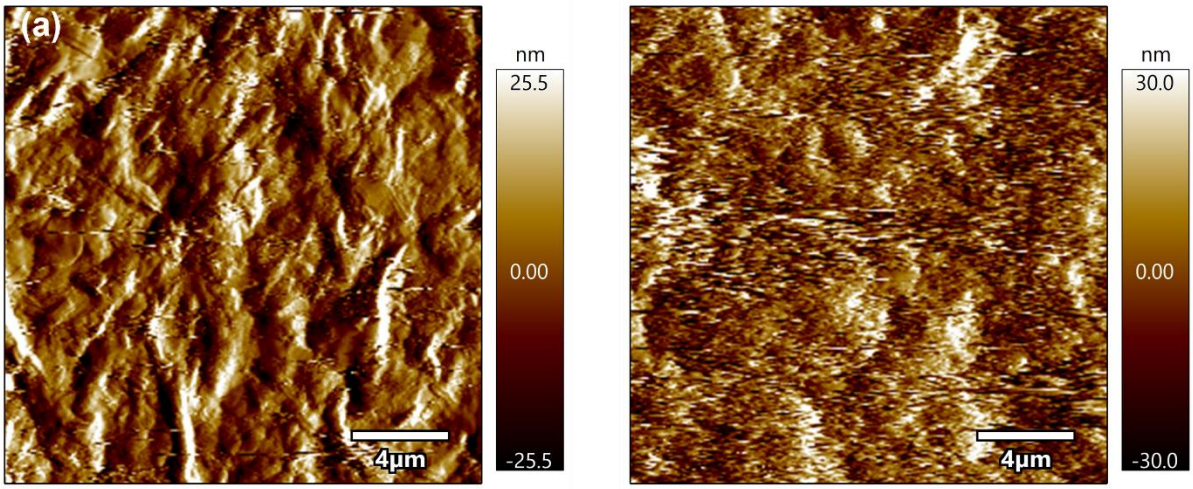

Figure S17. (a-b) AFM images of the (a) $Ni_3(HITP)_2$/MXene and (b) $Ni_3(HITP)_2$ films.

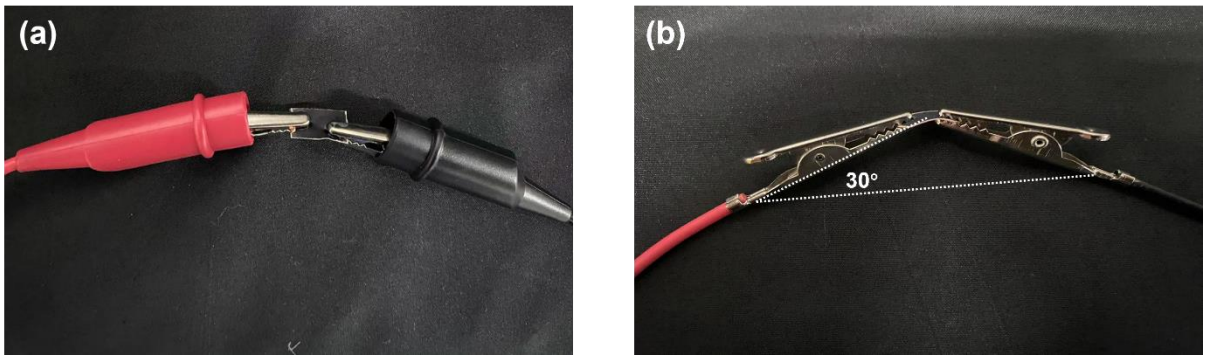

Figure S18. (a-b) Optical photograph of the $Ni_3(HITP)_2$/MXene films (a) before and (b) after bending at 30 degrees, corresponding to the schematic diagram in Figure 2h.

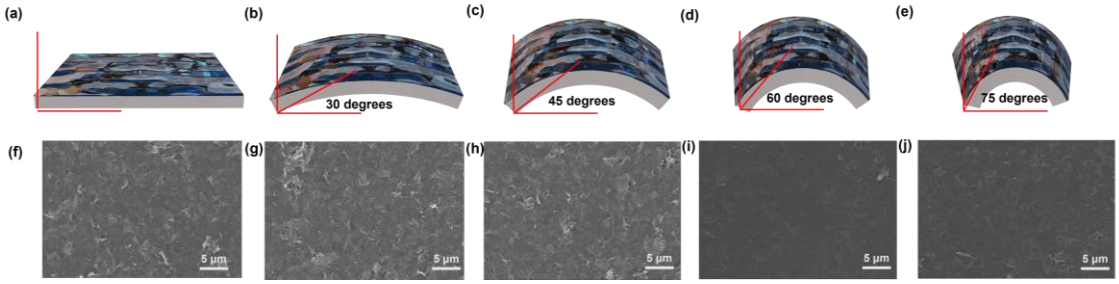

Figure S19 (a-e) Schematic bending diagram of $Ni_3(HITP)_2$/MXene films onto a flexible PVDF substrate before and after bending at different angles (0, 30, 45, 60, and 75 degrees) and their associated SEM images (f-j).

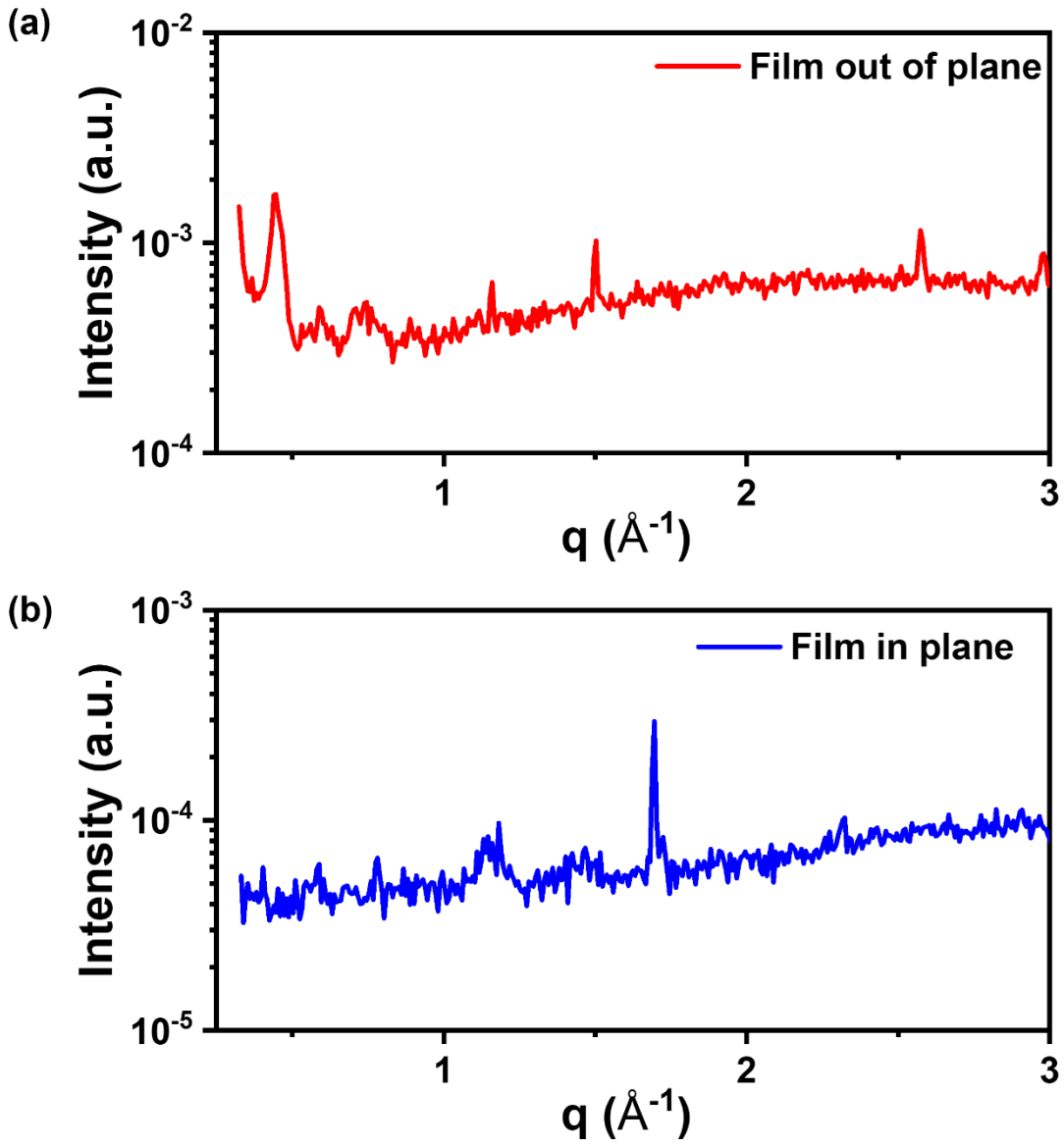

Figure S20. (a-b) Comparison of the out-of-plane and in-plane GIWAXS scattering profiles of the $Ni_3(HITP)_2$ film.

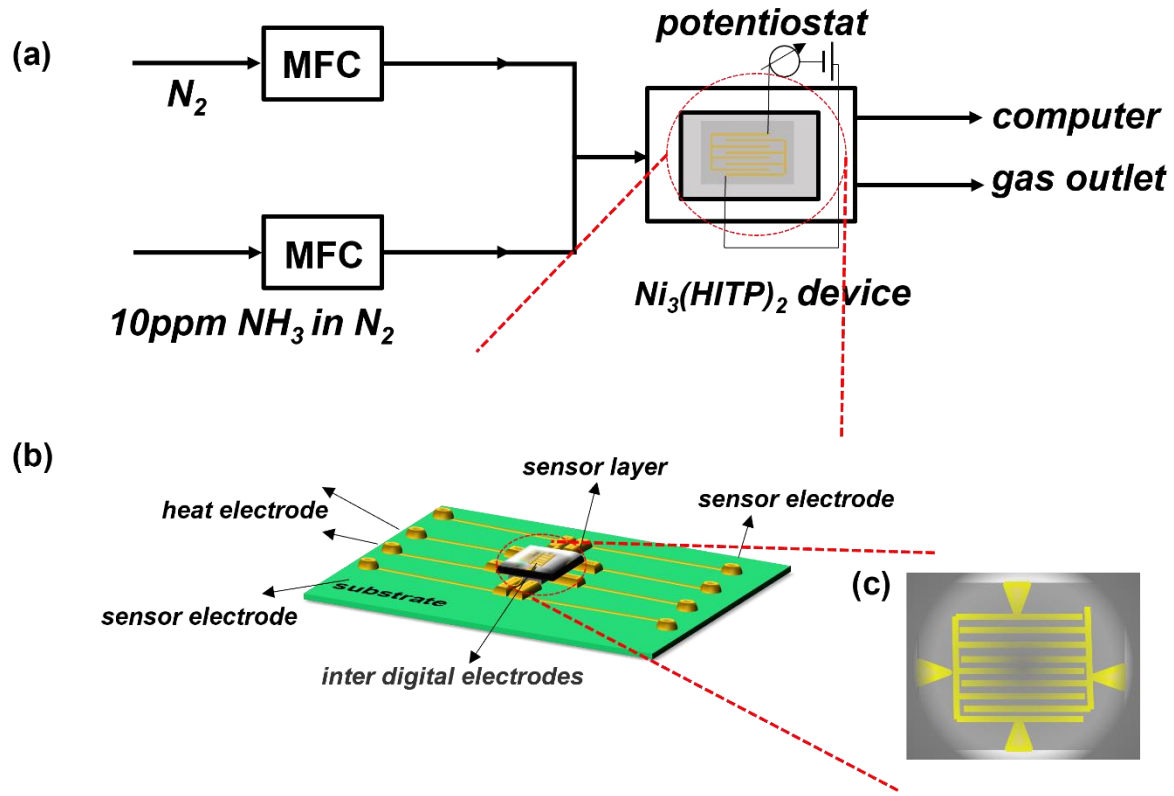

Figure S21. (a) Schematic diagram of the experimental apparatus. (b-c) Schematic diagram of the chip structure used within this study.

Note: The sensor performance of the sensors based on $Ni_3(HITP)_2$/MXene and $Ni_3(HITP)_2$ was evaluated using a homemade gas sensing system[S8]. The device was placed in the detection chamber, and the electrodes were connected to a digital multimeter. The entire experiment was conducted at room temperature. For typical experiments, the gas concentration and type were adjusted, and the resistance was monitored in real-time using a digital multimeter. The gas molecule concentration was accurately controlled by mass flow controllers (MFC). Before each test, the chamber was purged with nitrogen gas (N_2) for 15 minutes to stabilize the baseline resistance.

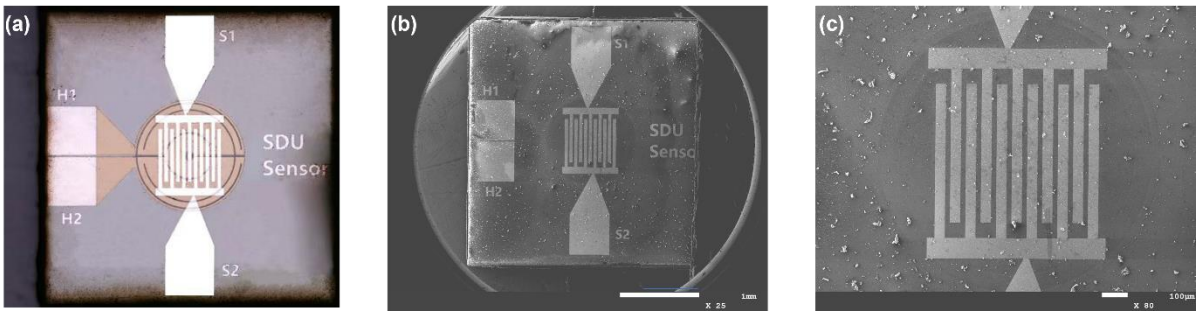

Figure S22. (a) Optical photographs of the sensor. (b-c) SEM images of the sensor.

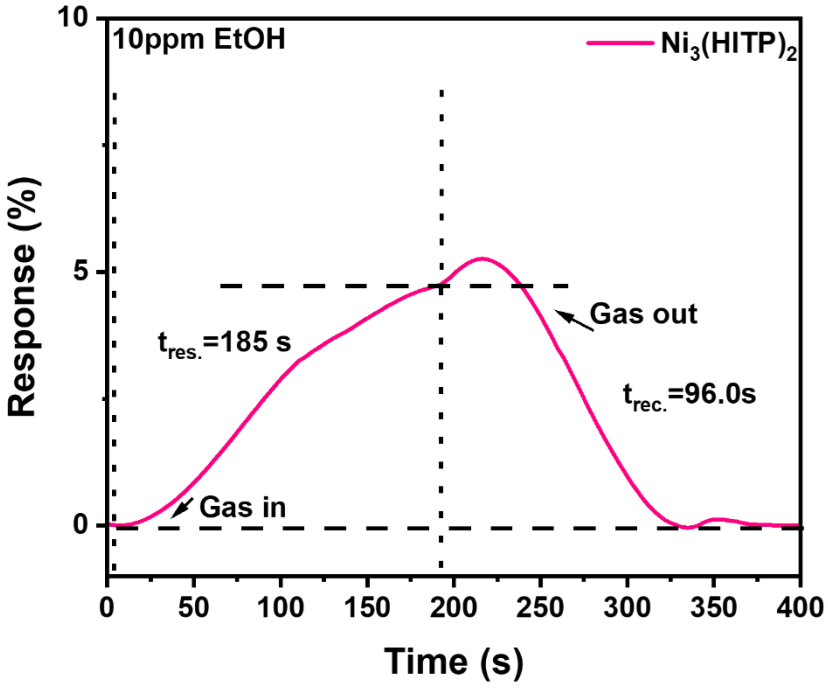

Figure S23. Dynamic response-recovery curve of the sensor based on $Ni_3(HITP)_2$ to 10 ppm EtOH.

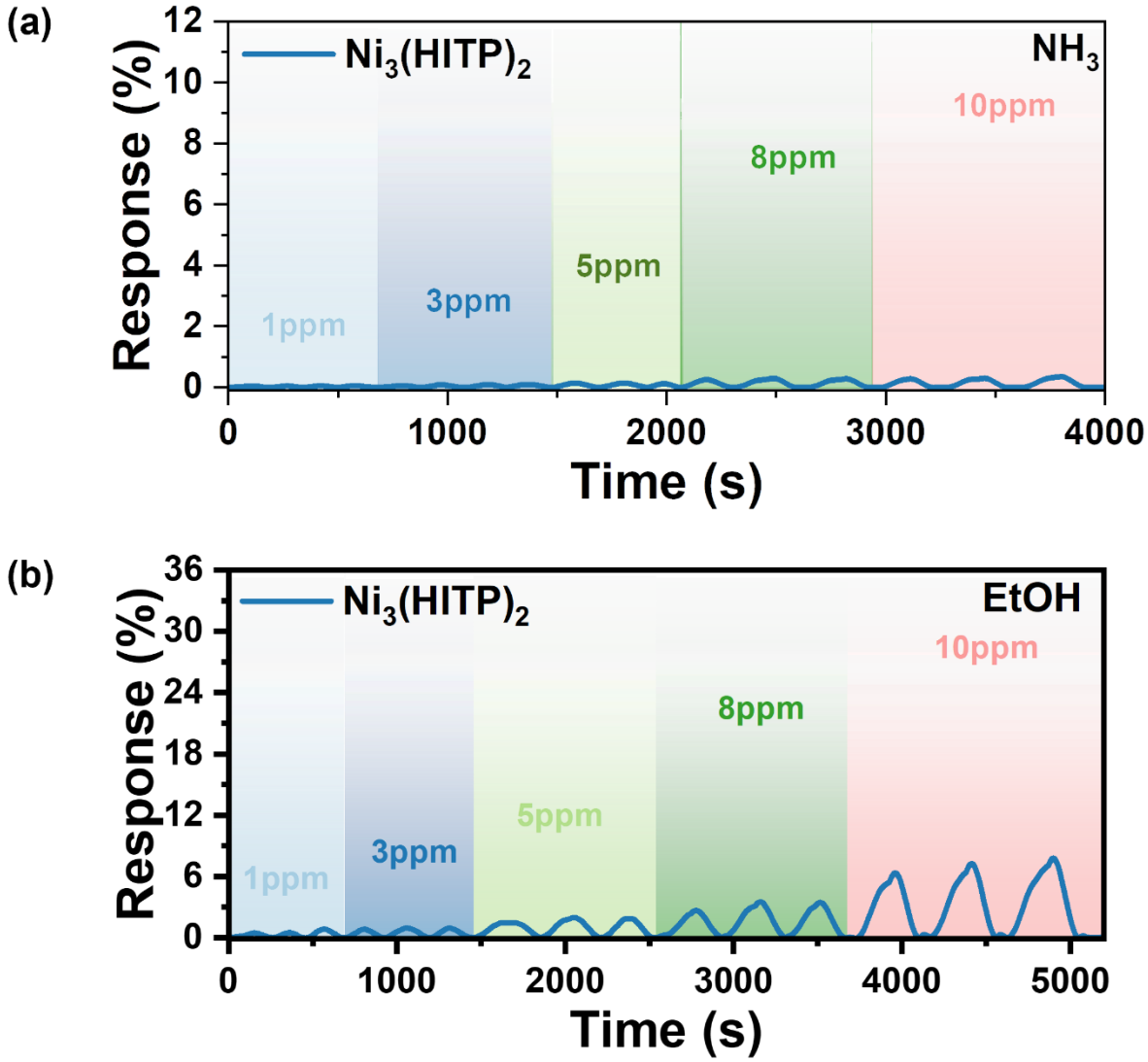

Figure S24. (a-b) Response-recovery curves of the $Ni_3(HITP)_2$ coated sensor to different concentrations of NH_3 and EtOH.

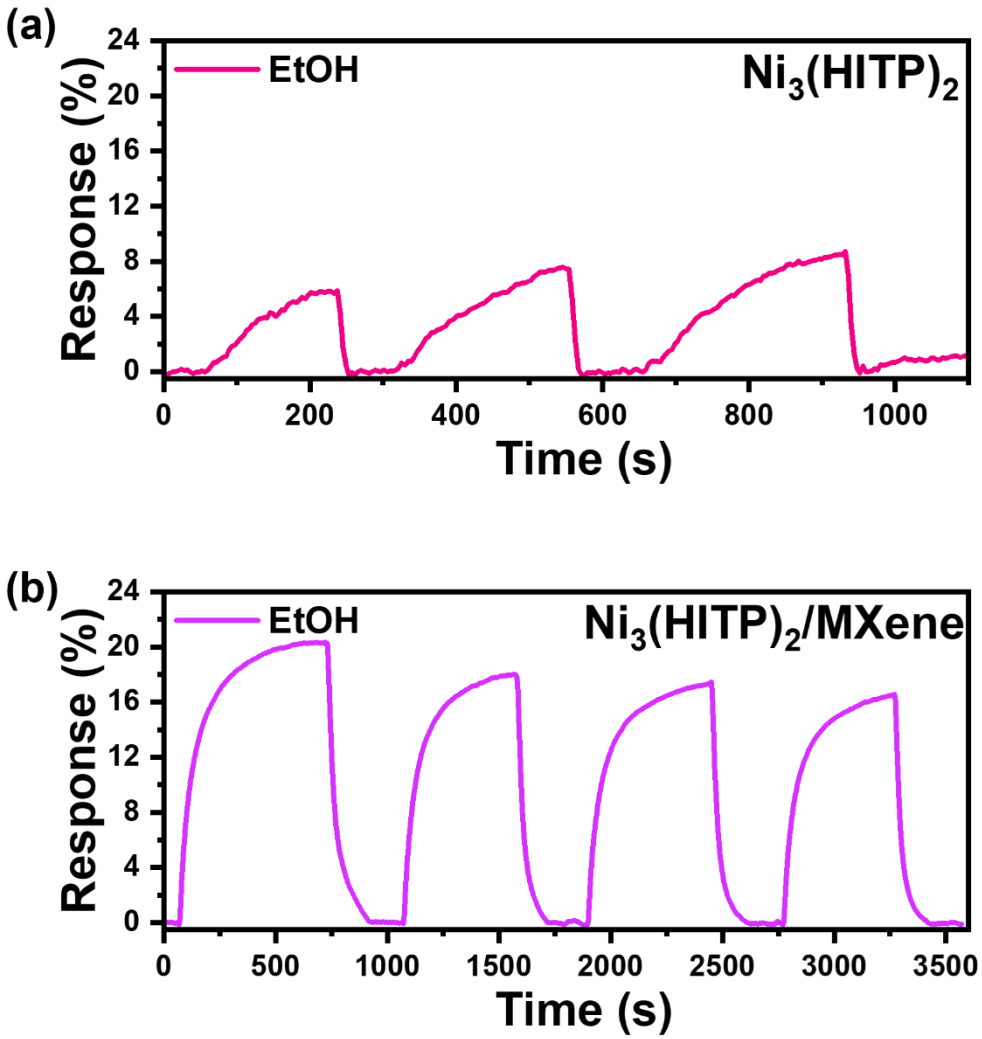

Figure S25. (a-b) Response-recovery curves of the sensors based on $Ni_3(HITP)_2$ and $Ni_3(HITP)_2$/MXene to 10 ppm EtOH, respectively.

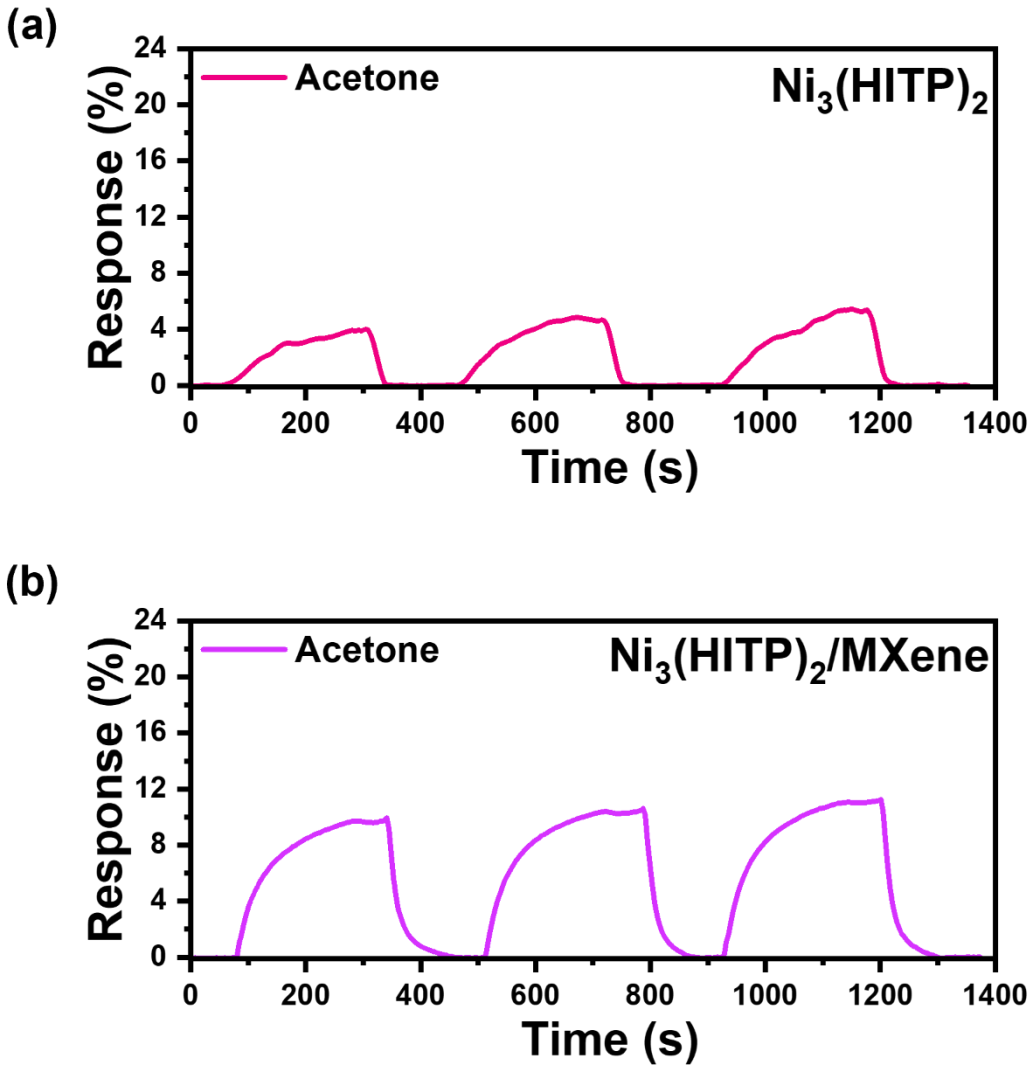

Figure S26. (a-b) Response-recovery curves of the sensors based on $Ni_3(HITP)_2$ and $Ni_3(HITP)_2$/MXene to 10 ppm acetone, respectively.

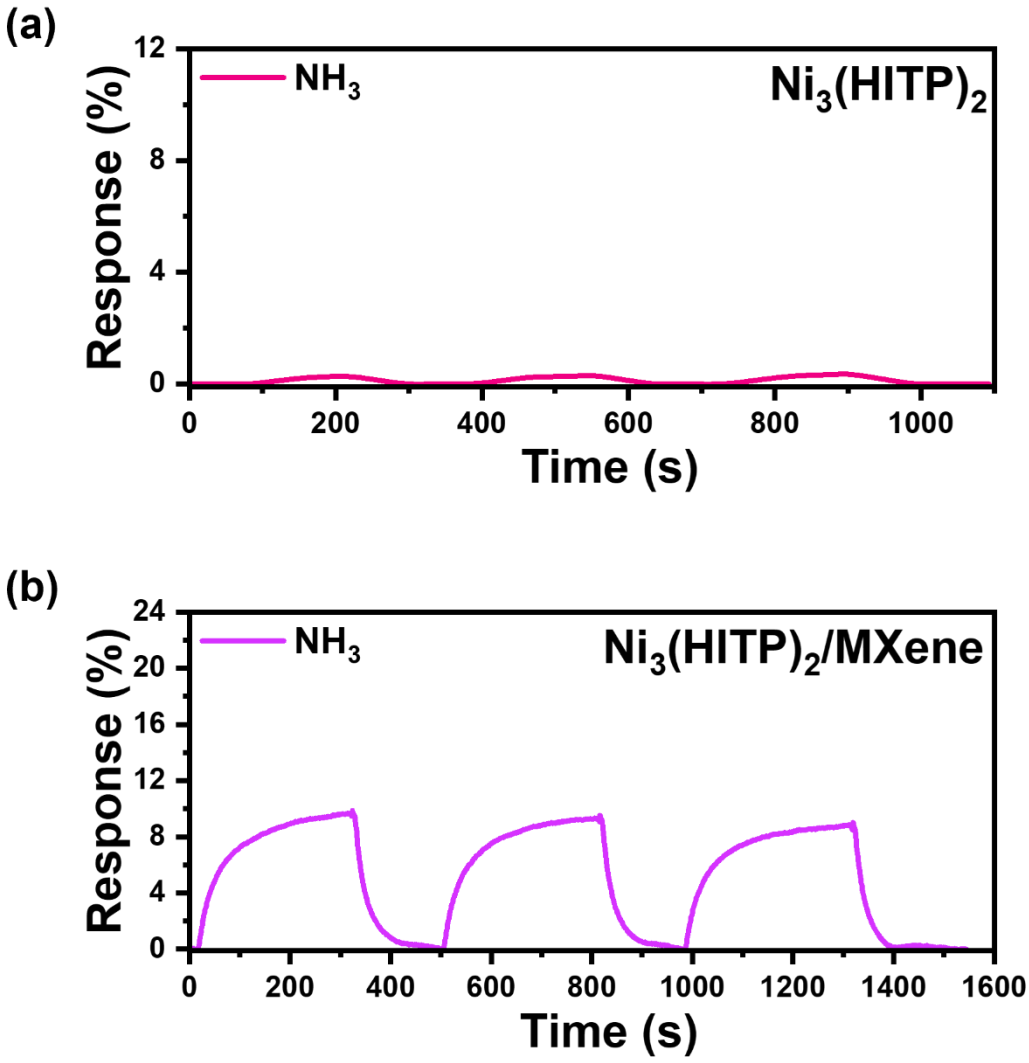

Figure S27. (a-b) Response-recovery curves of the sensors based on $Ni_3(HITP)_2$ and $Ni_3(HITP)_2$/MXene to 10 ppm NH_3, respectively.

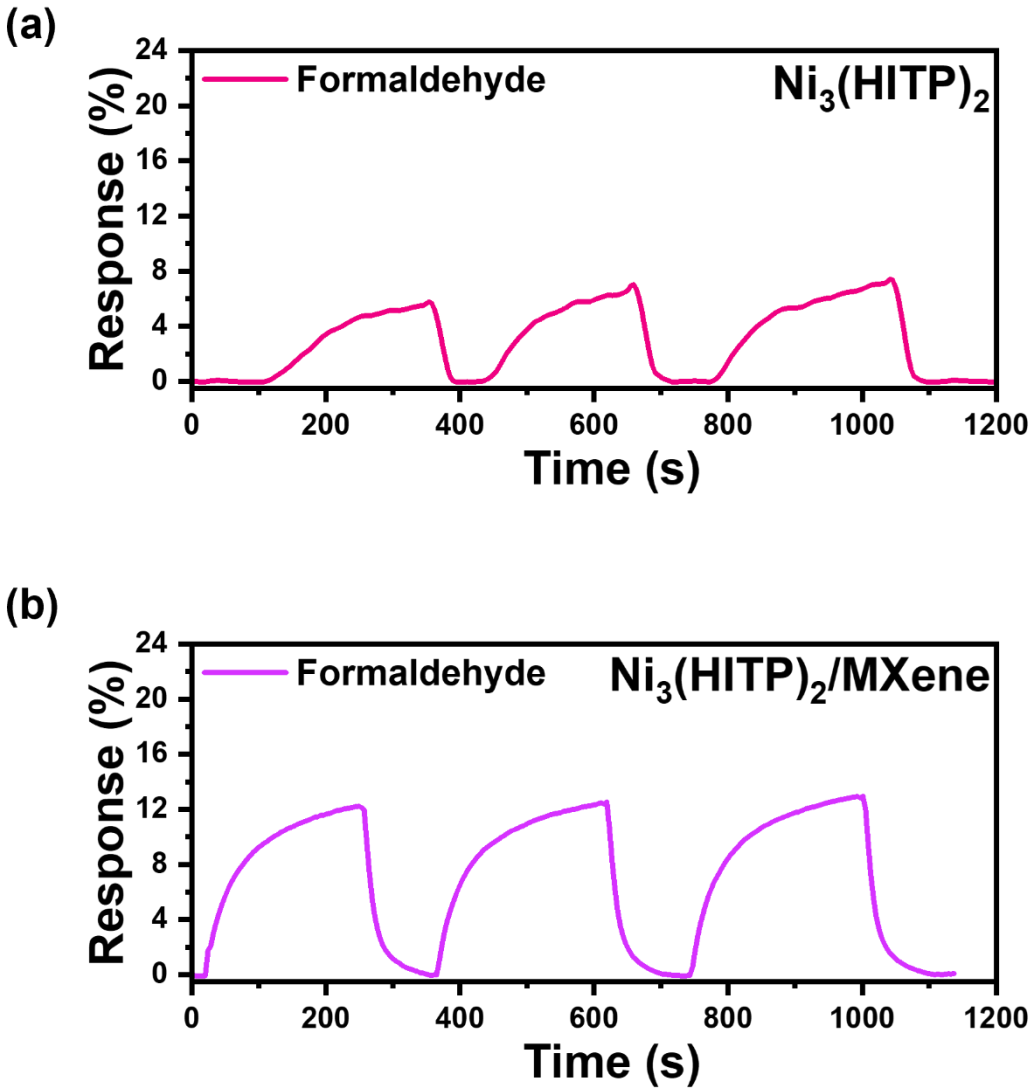

Figure S28. (a-b) Response-recovery curves of the sensors based on $Ni_3(HITP)_2$ and $Ni_3(HITP)_2$/MXene to 10 ppm formaldehyde, respectively.

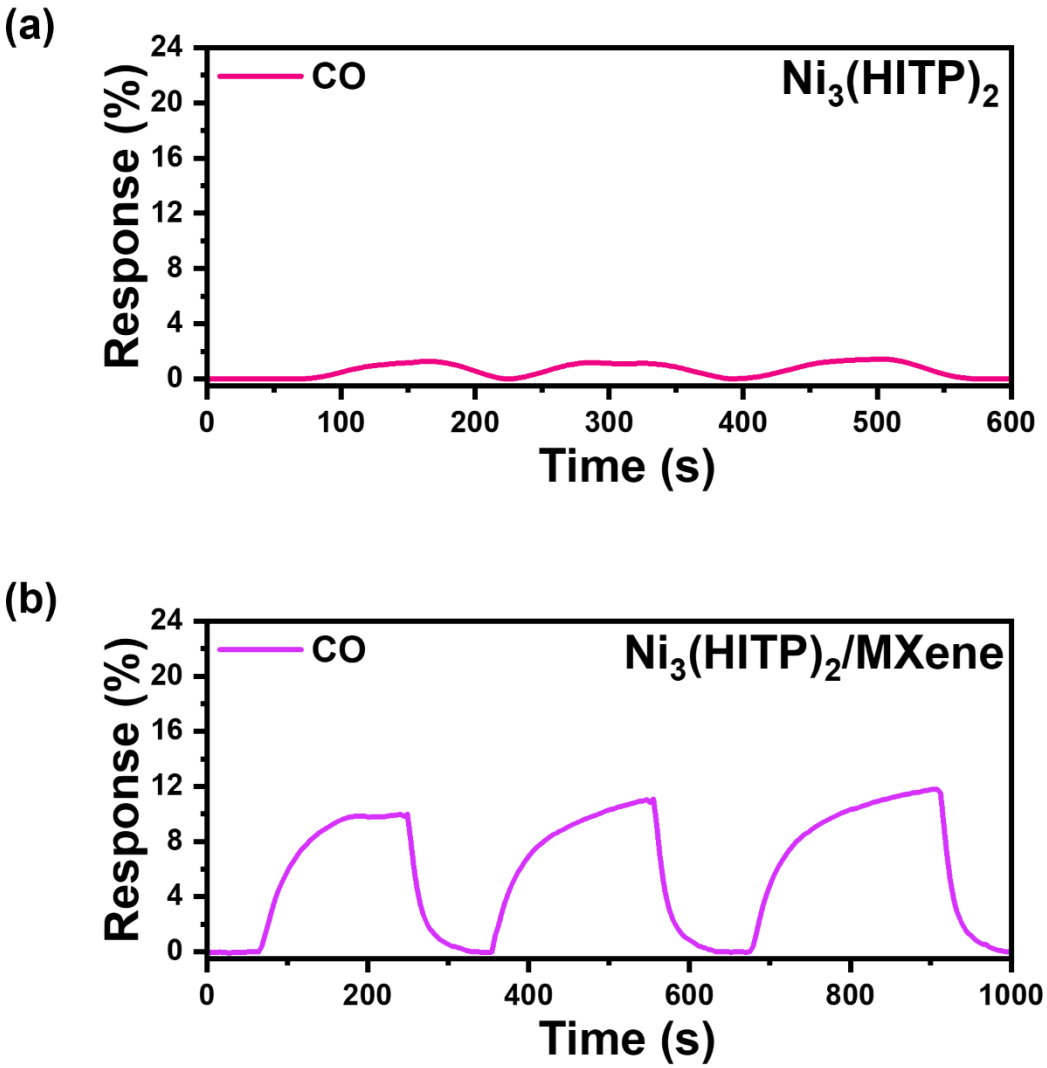

Figure S29. (a-b) Response-recovery curves of the sensors based on $Ni_3(HITP)_2$ and $Ni_3(HITP)_2$/MXene to 10 ppm CO, respectively.

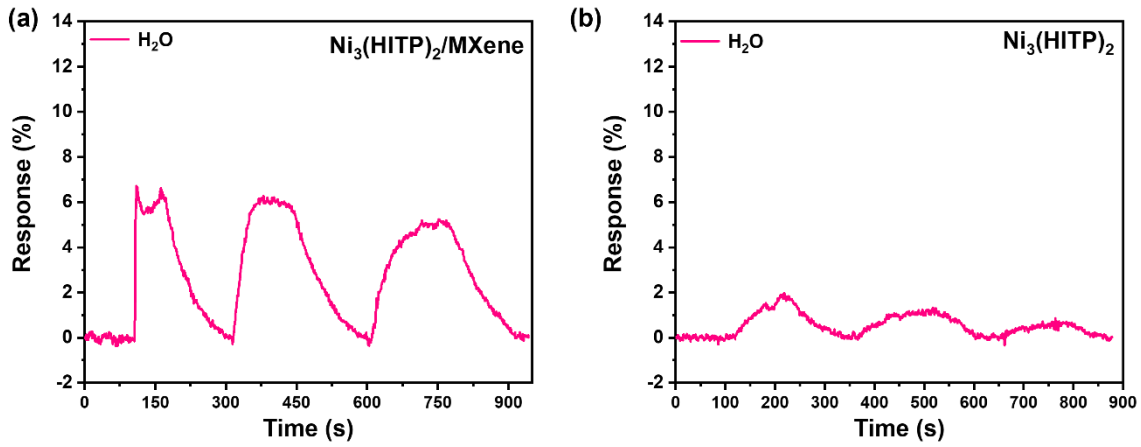

Figure S30. (a-b) Response-recovery curves of the sensors based on $Ni_3(HITP)_2$ and $Ni_3(HITP)_2$/MXene to 10 ppm water vapor, respectively.

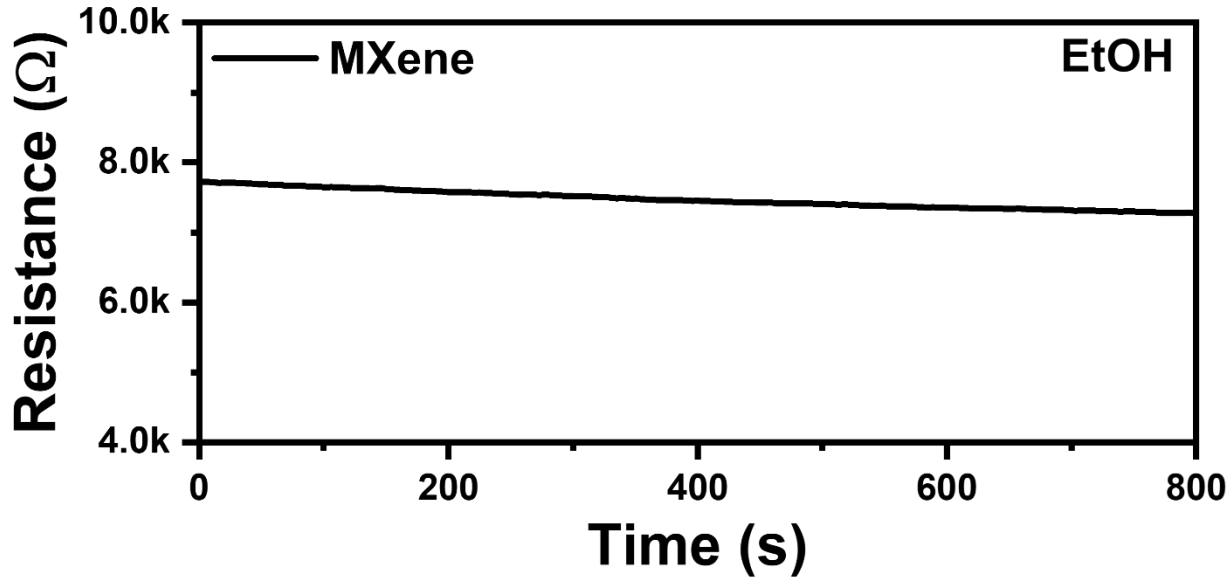

Figure S31. Resistance curve of the MXene coated sensor to 10 ppm EtOH.

Note: The MXene-based sensors did not exhibit a significant resistance response in the presence of 10 ppm EtOH.

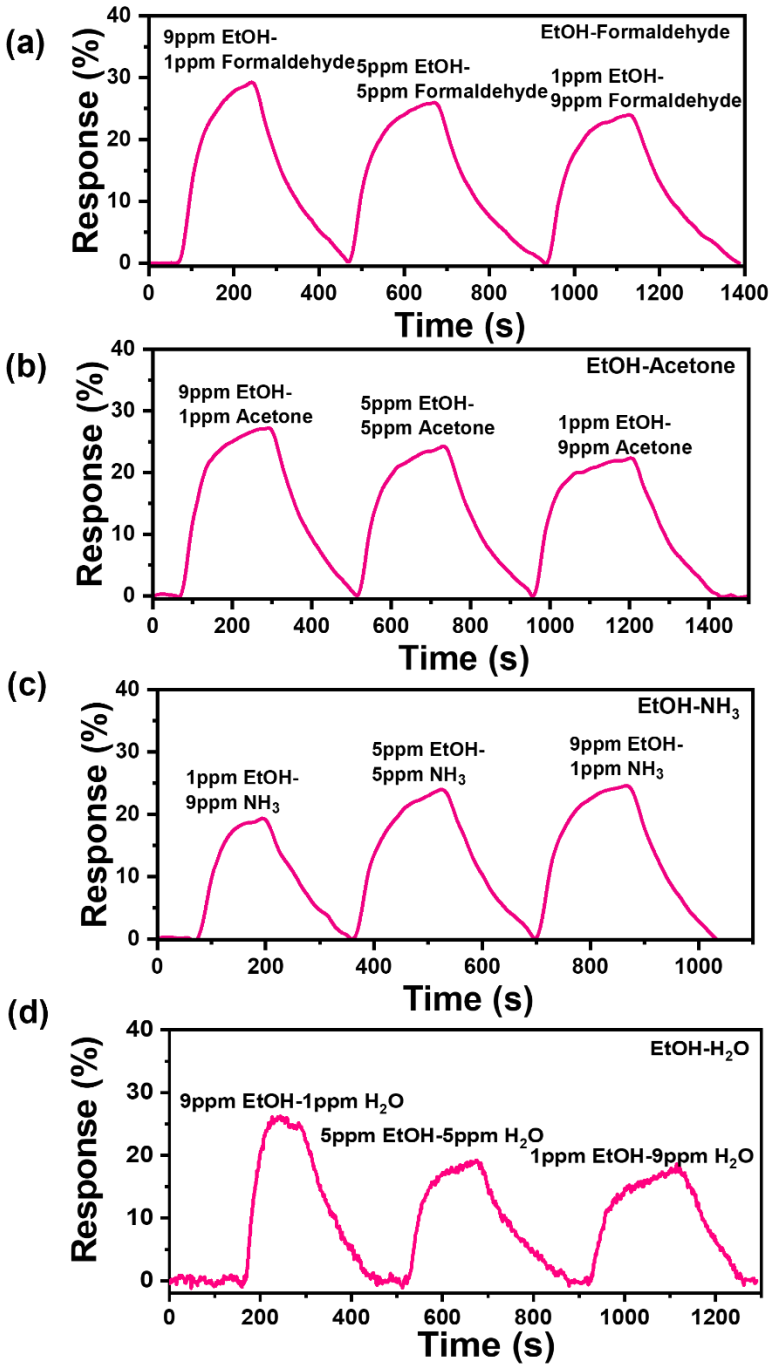

Figure S32. (a-d) Response-recovery curves of the $Ni_3(HITP)_2$/MXene coated sensors placed in mixed gas environments with different concentrations (1, 5, 9 ppm) and types (EtOH, acetone, formaldehyde, NH_3, H_2O).

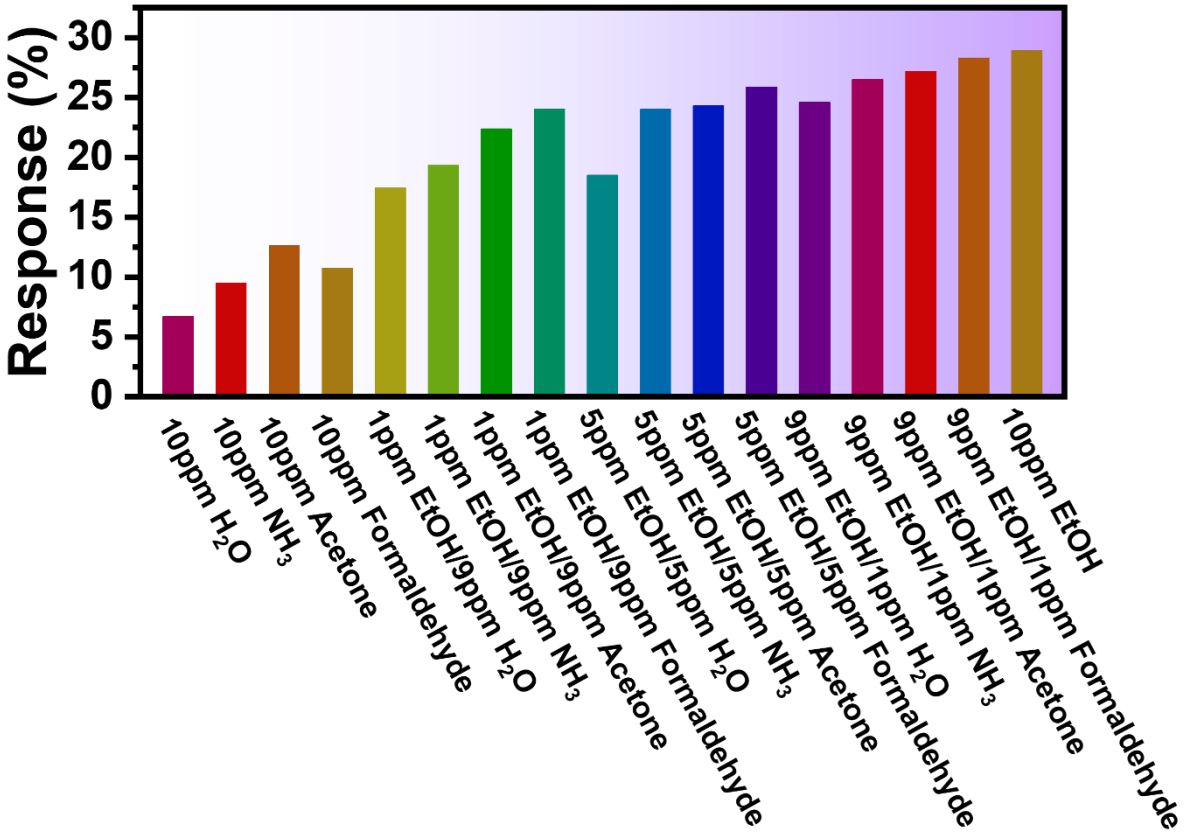

Figure S33. Bar graph of the response of the $Ni_3(HITP)_2$/MXene coated sensors placed in mixed gas environments with different concentrations (1, 5, 9 ppm) and types (EtOH, acetone, formaldehyde, NH_3, H_2O).

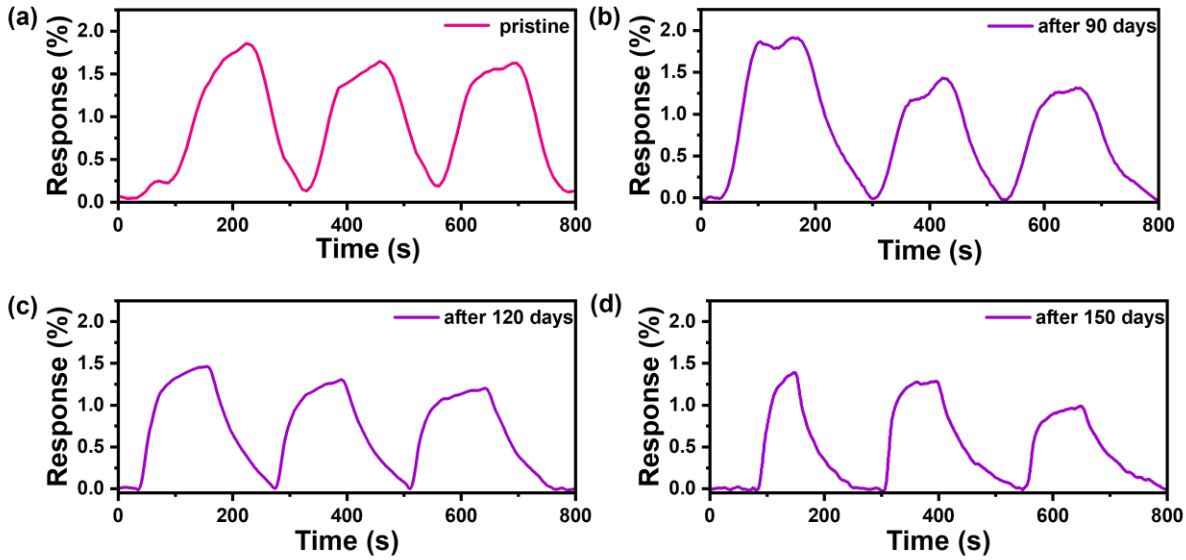

Figure S34. (a-d) Response-recovery curves of the $Ni_3(HITP)_2$/MXene coated sensors to 1 ppm EtOH after being stored for (a) 0, (b) 90, (c) 120, and (d) 150 days.

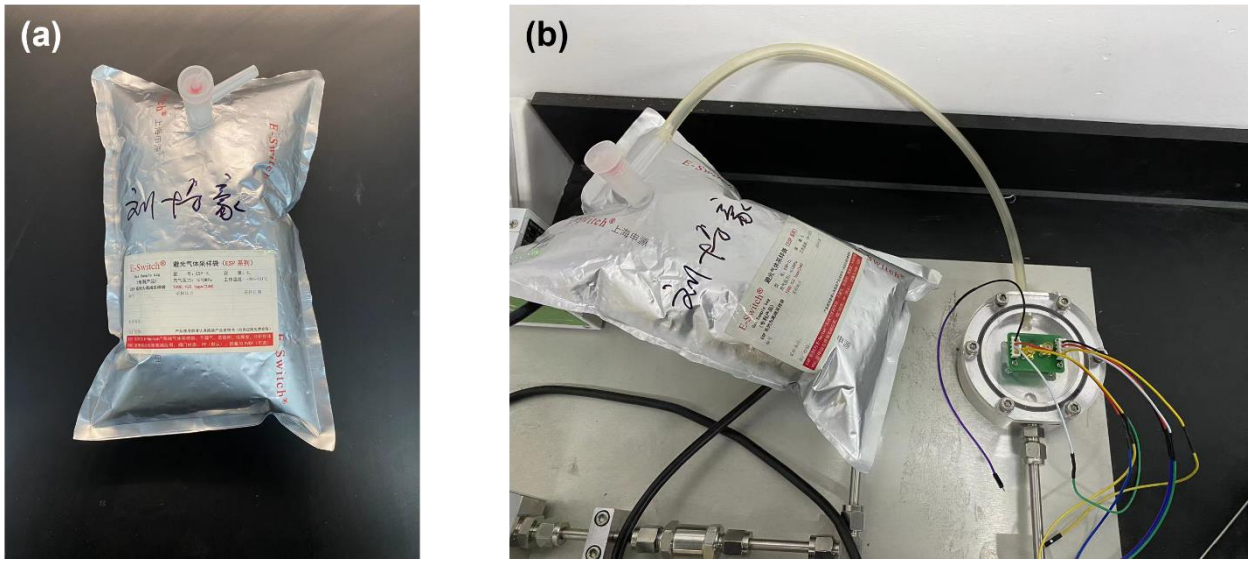

Figure S35. (a) Respiratory bags used to collect human respiratory gases. (b) The collection bag containing respiratory biomarker ethanol is connected to the customized room for sensing detection

Note: In the experiment, we employed a common method for collecting human breath gas, using a breath bag or breath sample collector, as illustrated in Figure S34. Participants were first instructed to consume alcohol for a specific duration, and then exhale into the breath bag or breath sample collector at specific time intervals. During the measurement process, the chip was placed within a custom chamber with stretchable metal contacts. The collection bag containing the breath biomarker ethanol was connected to the custom chamber. The relative changes in the target breath biomarker ethanol were evaluated by measuring the resistance change before and after gas adsorption. Additionally, before data acquisition, the chamber was purged with nitrogen gas (N_2) for 15 minutes to stabilize the baseline resistance. N_2 was also used as a diluent to achieve the target concentration and for sensor regeneration.

(a)

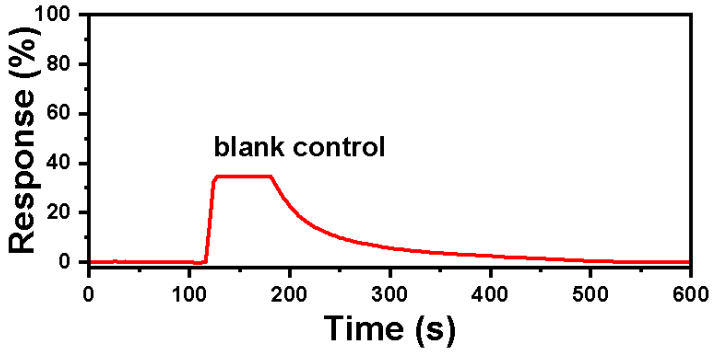
Response (%)
Time (s)
blank control

(b)

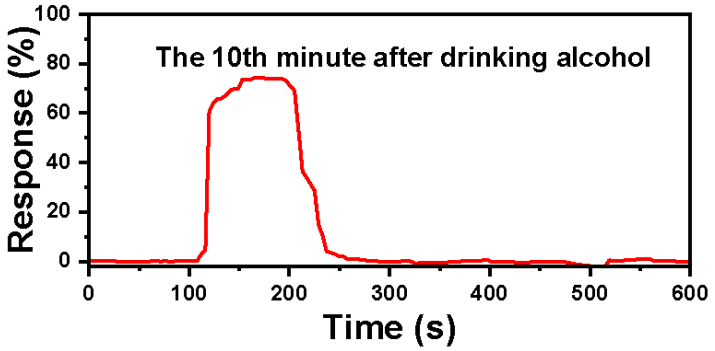
Response (%)
Time (s)
The 10th minute after drinking alcohol

(c)

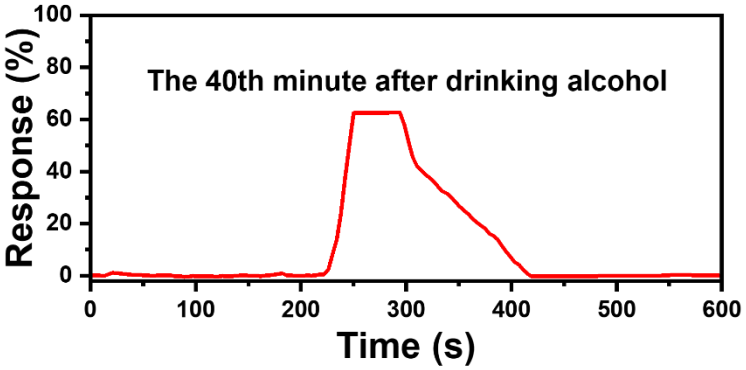
Response (%)
Time (s)
The 40th minute after drinking alcohol

(d)

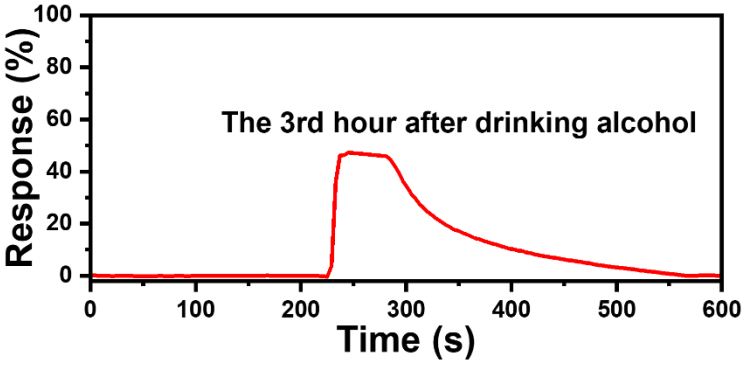
Response (%)
Time (s)
The 3rd hour after drinking alcohol

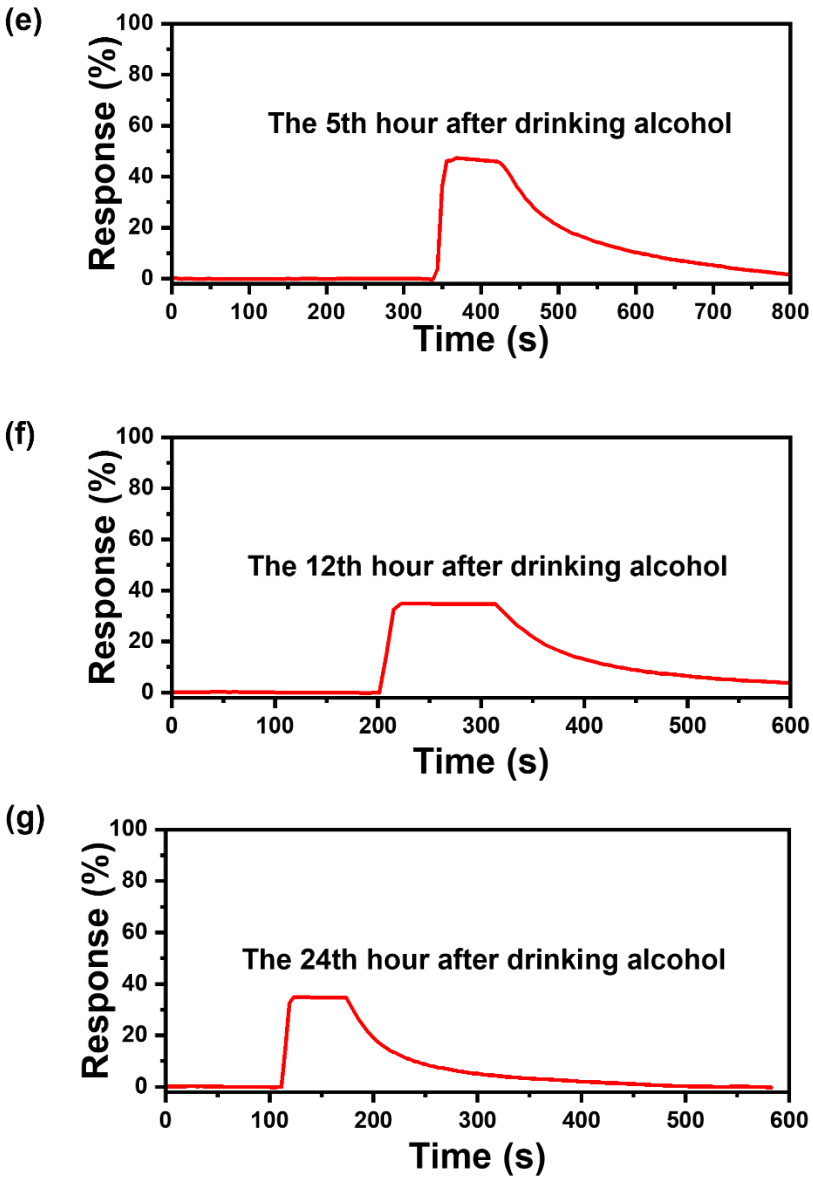

Figure S36. (a-g) Response-recovery curves of human breath after alcohol consumption at (a) 0 h, (b) 10 minutes, (c) 40 minutes, (d) 3 h, (e) 5 h, (f) 12 h, (g) 24 h.

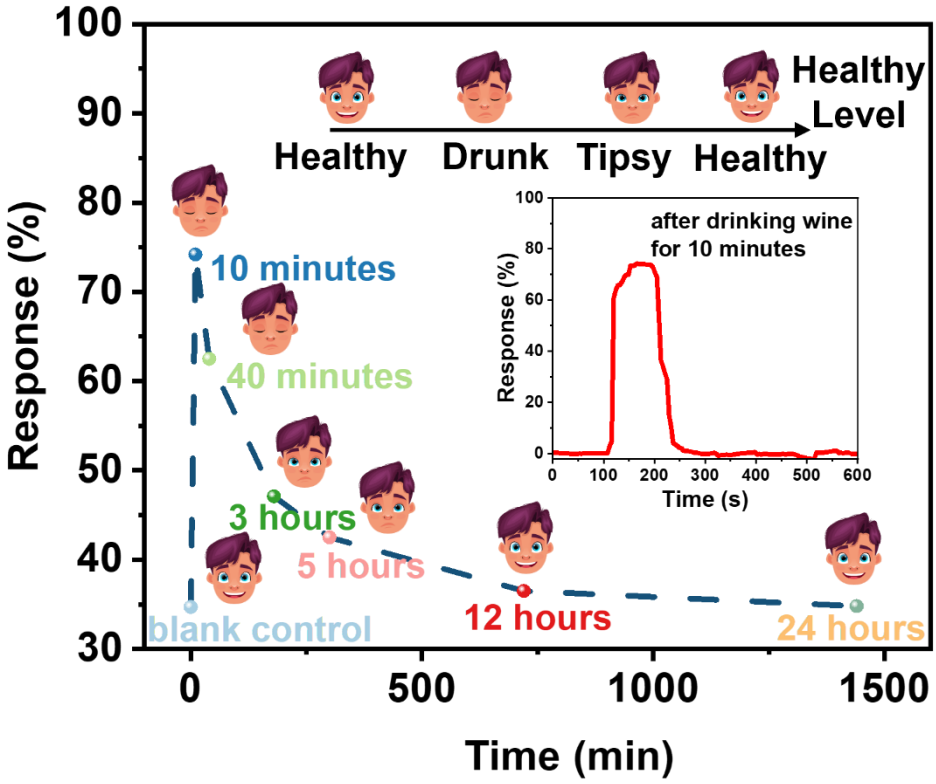

Figure S37. Real-time monitoring of human breath gas after alcohol consumption within 24 hours.

Note: In the experiment,we recorded real-time changes in human respiratory resistance within 24 hours after drinking alcohol. The results showed that compared to the baseline, there was a significant change in respiratory response within only 40 minutes after drinking alcohol, marking the beginning of the drunken state. Within the following 3-5 hours, the respiratory response gradually stabilizes, reflecting the individual's transition from a drunken state to a mildly intoxicated state. In the end, between 12-24 hours, the respiratory response was very similar to the baseline, indicating that the patient had returned to a normal state.

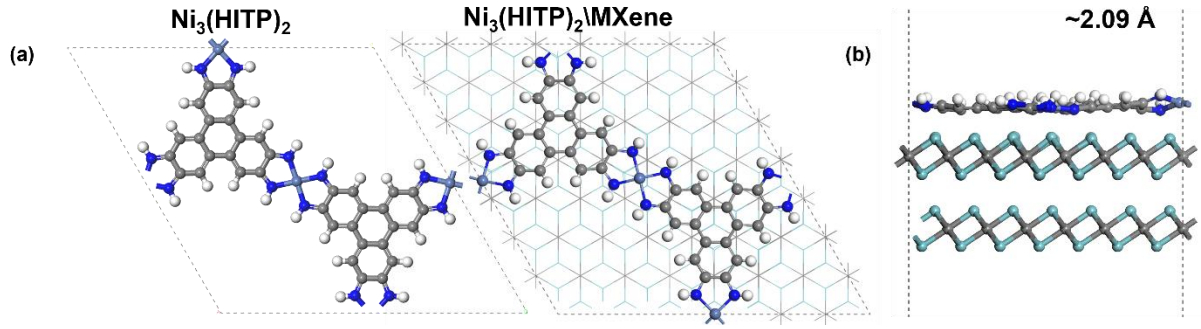

Figure S38. (a) Top view of the calculated $Ni_3(HITP)_2$ and $Ni_3(HITP)_2$/MXene heterostructure, respectively; (b) Side view of $Ni_3(HITP)_2$/MXene heterostructure after relaxing, respectively.

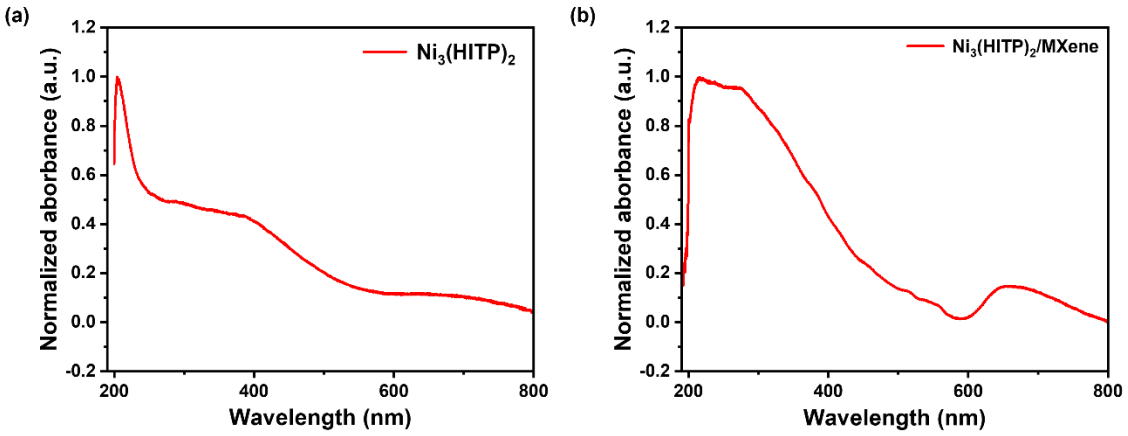

Figure S39. (a-b) UV-Vis absorption spectra of (a) $Ni_3(HITP)_2$ and (b) $Ni_3(HITP)_2$/MXene.

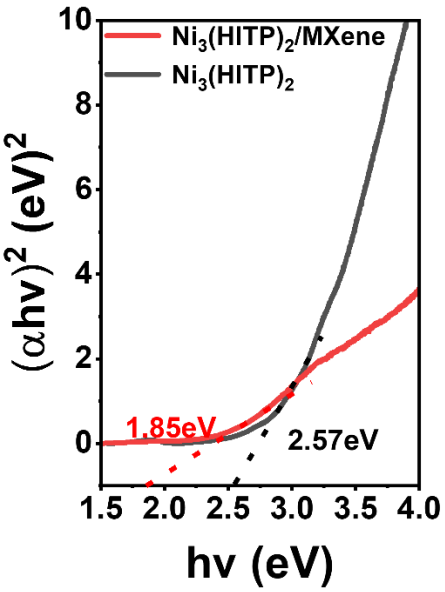

Figure S40. Calculated optical bandgaps of the $Ni_3(HITP)_2$/MXene and $Ni_3(HITP)_2$ based on UV-Vis spectra.

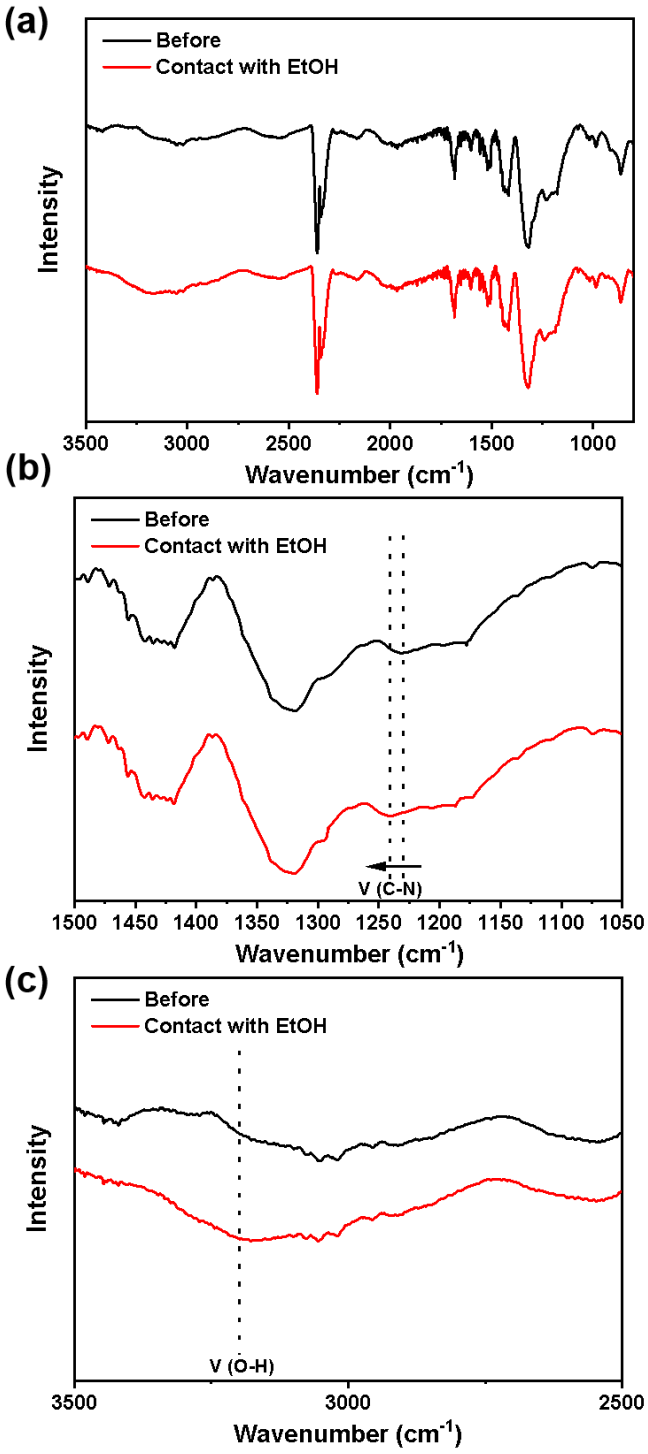

Figure S41. (a-c) FTIR spectra of the $Ni_3(HITP)_2$/MXene powder before and after adsorption of EtOH at relatively low concentration (10 ppm).

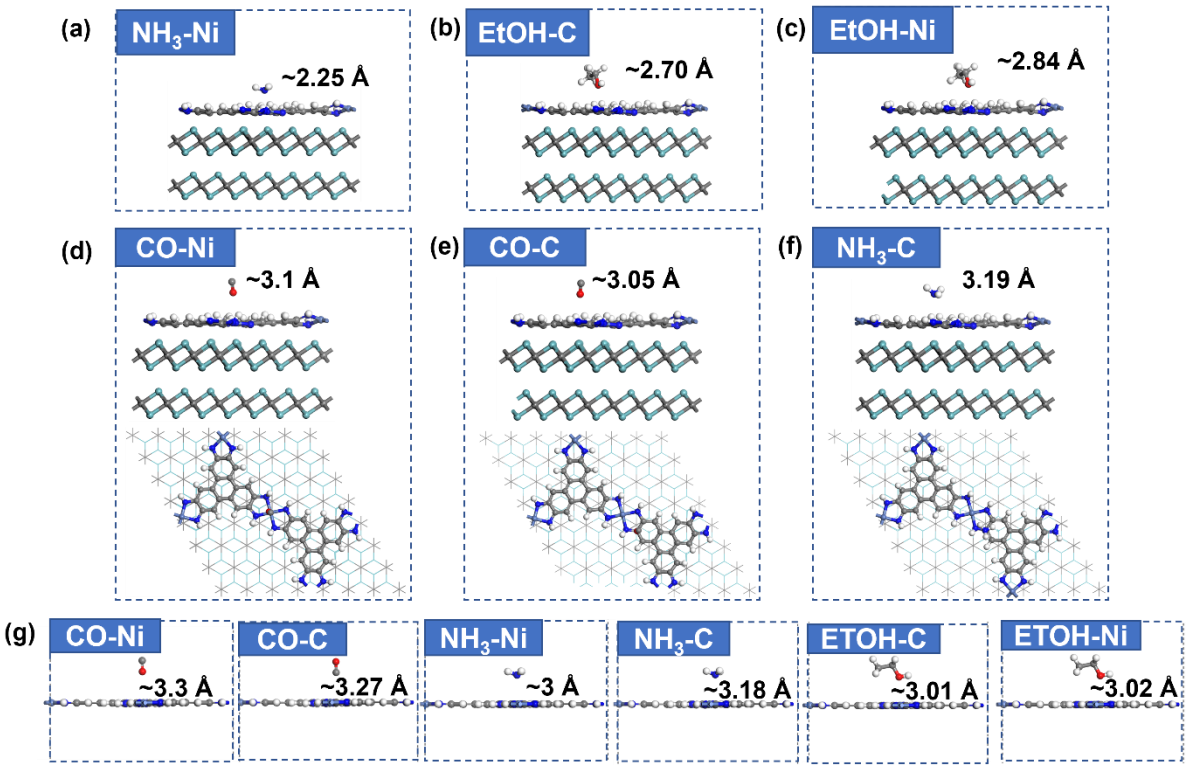

Figure S42. Physisorption of CO, NH_3 and EtOH on $Ni_3(HITP)_2$/MXene heterostructure and the monolayer $Ni_3(HITP)_2$. (a-f) Side and top views of the sensing molecules on $Ni_3(HITP)_2$/MXene heterostructure. (e) Side view of CO, NH_3 and EtOH on $Ni_3(HITP)_2$.

Table S1. Conductivity comparison of the $Ni_3(HITP)_2$/MXene with other materials in the literature. Note that the $Ni_3(HITP)_2$ film we prepared just by drop-casting shows a conductivity of 1.2 S m^{-1}, which is lower than that of the $Ni_3(HITP)_2$ pellet prepared by compression, highlighting the advantage of the solution processability of the resultant $Ni_3(HITP)_2$/MXene system.

Materials	State	Conductivity (S m^{-1})	Ref.
$Ni_3(HITP)_2$	**Powder**	**2.7×10^2**	**This work**
$Ni_3(HITP)_2$	**Film**	**1.2**	**This work**
$Ni_3(HITP)_2$/MXene	**Powder**	**4.8×10^3**	**This work**
$Ni_3(HITP)_2$/MXene	**Film**	**5.3×10^5**	**This work**
$Cu_3(HHTP)_2$	Powder	0.2	32
$Cu_3(HITP)_2$	Powder	20	33
$Ni_3(HHTP)_2$	Powder	10	34
NiPc-Ni	Powder	~7.2×10^{-2}	35
NiPc-Cu	Powder	1.4	35
Cu-HHTP-THQ	Powder	~ 2.5×10^{-3}	35
ZIF-8/rGO	Powder	64	37
ZIF-8/SWCNT	Powder	5.6	38
UiO-66/CNT	Powder	~ 1.25×10^3	39
MOF/PEDOT	Powder	0.7	40
MOF/ppy	Powder	~ 1.15×10^2	41
$La_4(HTTFTB)_4$ (1)	Powder	5.4×10^{-4}	S13
La(HTTFTB) (2)	Powder	2.7×10^{-4}	S13
$La_4(TTFTB)_3$ (3)	Powder	3.1×10^{-7}	S13
LaHHTP	Powder	0.9×10^{-2}	S14
HoHHTP	Powder	5.0	S14

DDA-Cu	Powder	9.4	S15
c-HBC-12O-Cu	Powder	3.31	S16
Cu_4DHTTB	Powder	20	S17
Cu_2(OHPTP)	Powder	10	S18
Ni_3(HATI_C1)$_2$	Powder	1.1	S19
Ni_3(HATI_C3)$_2$	Powder	0.45	S19
Ni_3(HATI_C4)$_2$	Powder	0.09	S19
Ni-CAT-1-on-SLG	Film	4×10^4	27
Co_9(HOTP)$_4$	Film	0.33	S20
Cu_3(HOTP)$_2$	Film	29	S20
Fe_3(THT)$_2$(NH_4)$_3$	Film	3.4	S20
Ag_3(BHT)$_2$	Film	3.6×10^4	S20
Ni_3(BHT)$_2$	Film	1.6×10^4	S20
Ni_2[Ni(IPc)]	Film	0.2	S20
Ni/Fe(NDC)	Film	1.0×10^{-3}	S20
Cu_3(BTC)$_2$ (HKUST-1)	Film	7.0	S20

Table S2. Sensing performance comparison the gas sensors based on $Ni_3(HITP)_2$/MXene with other ones based on pure MOF or MOF-based composite materials, and most MOS-based sensors to EtOH and NH_3.

Materials	T (℃)	Gas	Conc. (ppm)	Response (%)	LOD (ppm)	Ref.
$Ni_3(HITP)_2$	**RT**	**NH_3**	**10**	**0.25**	**N.A.**	**This work**
$Ni_3(HITP)_2$	**RT**	**EtOH**	**10**	**6.05**	**0.48**	**This work**
$Ni_3(HITP)_2$/MXene	**RT**	**NH_3**	**10**	**9.46**	**0.25**	**This work**
$Ni_3(HITP)_2$/MXene	**RT**	**EtOH**	**10**	**28.8**	**0.005**	**This work**
CuTCNQ	RT	NH_3	50	0.1	10	31
$CuTCNQF_4$	RT	NH_3	99	4.34	10	31
$Cu_3(HHTP)_2$	RT	NH_3	80	0.7	2	32
$Cu_3(HITP)_2$	RT	NH_3	10	3	0.5	33
$Ni_3(HHTP)_2$	RT	NH_3	80	0	0	32
NiPc-Ni	RT	NH_3	80	~45	0.05–0.31	35
NiPc-Cu	RT	NH_3	80	~45	0.16–0.33	35
Cu-HHTP-THQ	RT	NH_3	100	20	0.02	36
Cu-BTC@GO-25	RT	NH_3	100	4	100	52
Ni-CAT-1-on-SLG	RT	NH_3	100	6.75	0.01	27
SnS_2−SnO_2	RT	NH_3	10	1.2	10	56
$Ti_3C_2T_x$	RT	NH_3	100	0.8	1.3×10^{-4}	57
ZnO@ZIF-8@POM	RT	EtOH	100	30	N.A.	55
$Cu_3(HHTP)_2$ (thick film)	RT	EtOH	200	2.3	N.A.	54
$Cu_3(HHTP)_2$ (thin film)	RT	EtOH	100	40	N.A.	40
Cu_3 $(HITP)_2$	RT	EtOH	200	0.8	N.A.	44
CuO	260	EtOH	10	1.6	N.A.	S9
Gr−Fe_2O_3	280	EtOH	1	4.8	N.A.	S9
MoO_3	300	EtOH	100	32.4	N.A.	S9
MoS_2	RT	EtOH	1	2	1	S10
SnO_2	300	EtOH	100	55	N.A.	S9
$Ti_3C_2T_x$	RT	EtOH	100	1.7	N.A.	S11
Co-TCPP(Fe)/$Ti_3C_2T_x$-20	RT	EtOH	20	1.01	N.A.	S12

Table S3. Adsorption energies and distances of $Ni_3(HITP)_2$/MXene and $Ni_3(HITP)_2$ for EtOH, NH_3, and CO. E_{ad} is the adsorption energy and Δd is the distance between gas molucules and subsrate.The unit of E_{ad} and Δd is eV and Å, respectively.

	CO-Ni	CO-C	NH_3-Ni	NH_3-C	EtOH-Ni	EtOH-C
E_{ad} ($Ni_3(HITP)_2$)	-0.06	-0.10	-0.03	-0.08	-0.12	-0.15
Δd	3.30	3.27	3.00	3.18	3.02	3.01
E_{ad}($Ni_3(HITP)_2$/MXene)	-0.09	-0.13	-0.37	-0.25	-0.34	-0.32
Δd	3.10	3.05	2.25	3.19	2.84	2.70

References

S1. H. Yuan, S. A. A. A. Aljneibi, J. Yuan, Y. Wang, H. Liu, J. Fang, C. Tang, X. Yan, H. Cai, Y. Gu, S. J. Pennycook, J. Tao, D. Zhao, *Adv. Mater*. 2019, **31**, 1807161.

S2. P. E. Blöchl, *Phys. Rev. B* 1994, **50**, 17953.

S3. G. Kresse, D. Joubert, *Phys. Rev. B* 1999, **59**, 1758.

S4. G. Kresse, J. Furthmüller, *Phys. Rev. B* 1996, **54**, 11169.

S5. G. Kresse, J. Furthmüller, *Comput. Mater. Sci.* 1996, **6**, 15.

S6. J. Klimeš, D. R. Bowler, A. Michaelides, *Phys. Rev. B* 2011, **83**, 195131.

S7. S. Homayoonnia, S. Zeinali, *Sens. Actuators. B* 2016, **237**, 776-786.

S8. H. Yuan, J. Tao, N. Li, A. Karmakar, C. Tang, H. Cai, S. J. Pennycook, N. Singh, D. Zhao, *Angew. Chem. Int. Ed*. 2019, **58**, 14089.

S9. Z. Meng, R. M. Stolz, L. Mendecki, K. A. Mirica, *Chem Rev*. 2019, **119**, 478.

S10. P. Dwivedi, S. Das, S. Dhanekar, *ACS Appl. Mater. Interfaces* 2017, **9**, 21017.

S11. E. Lee, A. VahidMohammadi, B. C. Prorok, Y. S. Yoon, M. Beidaghi, D. J. Kim, *ACS Appl. Mater. Interfaces* 2017, **9**, 37184-37190.

S12. Y. Chang, M. Chen, Z. Fu, R. Lu, Y. Gao, F. Chen, H. Li, N. F. Rooij, Y. Lee, Y. Wang, G. Zhou, *J. Mater. Chem. A* 2023, **11**, 6966-6977.

S13. L. S. Xie, E. V. Alexandrov, G. Skorupskii, D. M. Proserpio, M. Dincă, *Chem. Sci*. 2019, **10**, 8558-8565.

S14. G. Skorupskii, B. A. Trump, T. W. Kasel, C. M. Brown, C. H. Hendon, M. Dincă, *Nat. Chem.* 2020, **12**, 131–136.

S15. S. Shang, C. Du, Y. Liu, M. Liu, X. Wang, W. Gao, Y. Zou, J. Dong, Y. Liu, J. Chen, *Nat. Commun.* 2022, **13**, 7599.

S16. G. Xing, J. Liu, Y. Zhou, S. Fu, J. Zheng, X. Su, X. Gao, O. Terasaki, M. Bonn, H. Wang, L. Chen, *J. Am. Chem. Soc.* 2023, **145**, 8979−8987.

S17. X. Huang, S. Fu, C. Lin, Y. Lu, M. Wang, P. Zhang, C. Huang, Z. Li, Z. Liao, Y. Zou, J. Li, S. Zhou, M. Helm, P. S. Petkov, T. Heine, M. Bonn, H. Wang, X. Feng, R. Dong, *J. Am. Chem. Soc.* 2023, **145**, 2430–2438.

S18. L. Sporrer, G. Zhou, M. Wang, V. Balos, S. Revuelta, K. Jastrzembski, M. Löffler, P. Petkov, T. Heine, A. Kuc, E. Cánovas, Z.; Huang, X. Feng, R. Dong, *Angew. Chem. Int. Ed.* 2023, **62**, e202300186.

S19. Y. Lu, Y. Zhang, C. Yang, S. Revuelta, H. Qi, C. Huang, W. Jin, Z. Li, V. Vega-Mayoral, Y. Liu, X. Huang, D. Pohl, M. Položij, S. Zhou, E. Cánovas, T. Heine, S. Fabiano, X. Feng, R. Dong, *Nat. Commun.* 2022, **13**, 7240.

S20. L. S. Xie, G. Skorupskii, M. Dincă, *Chem. Rev.* 2020, **120**, 8536−8580.